PNAS

# Supplementary Information for
A complete biomimetic iron-sulfur cubane redox series

Liam Grunwald, Martin Clémancey, Daniel Klose, Lionel Dubois, Serge Gambarelli, Gunnar Jeschke, Michael Wörle, Geneviève Blondin and Victor Mougel*.

*Corresponding Author: Victor Mougel.
**Email:** mougel@inorg.chem.ethz.ch

**This PDF file includes:**

**Materials and Methods**

General Considerations:

Unless stated otherwise, syntheses were carried out strictly under inert Argon atmosphere using Schlenk techniques or inside Vigor® gloveboxes, ensuring oxygen and water levels were kept at all time below 1 ppm. Pentane was stirred over concentrated sulfuric acid, rinsed with aqueous bicarbonate solution and deionized water and dried over Calcium chloride beads before being used in a solvent purification system. Diethyl ether, toluene and pentane were dried using a Vigor® solvent purification system. Diethyl ether was additionally dried over potassium/benzophenone, distilled, degassed by 3 freeze-pump-thaw cycles and stored over molecular sieves for at least 3 days prior to use. Likewise, toluene and pentane were degassed by 4 freeze-pump-thaw cycles and stored over molecular sieves prior to use. HMDSO and diisopropylether were refluxed over sodium/benzophenone for at least 24 hours, distilled, degassed by 3 freeze-pump-thaw cycles and stored over 4 Å molecular sieves. [$FeHMDS_2$] (1), TripSH (2,4,6-triisopropylphenylthiol) (2), 2,6-dibromo-1-iodobenzene (3), [$Fe(DmpS)(TripS)]_2$ (4) and $KC_8$ (5) were prepared according to procedures reported in literature. Elemental sulfur, $S_8$, and LiHMDS were sublimed under high vacuum ($<10^{-6}$ mBar) prior to use. [$^n$$Bu_4$N][$BF_4$] and [$^n$$Bu_4$N][$PF_6$] were recrystallized from hot EtOH twice. K[$BArF_{24}$] was synthesized according to literature procedure (6) and recrystallized 8 times from a solution in THF/DCM (1:1) layered with hexane. Unless stated otherwise, reagents were used without special purification. Details of synthetic procedures and spectroscopic measurements, as well as additional characterization data for compounds **1**-**7** are provided below.

Spectroscopic Measurements:

For *X-band perpendicular-mode EPR spectra,* samples were transferred into 3 mm quartz capillaries (Quartzglas Heinrich, Aachen, Germany) fitted with custom-made Schlenk glass connections and flame-sealed on a Schlenk line under vacuum.
Continuous-wave (cw) EPR spectra were recorded on Elexsys E500 or E580 EPR spectrometers (Bruker Biospin, Rheinstetten, Germany) equipped with an ESR-900 helium flow cryostat (Oxford Instruments, Oxfordshire, UK) and a Super-High-Q resonator (Bruker) at ca. 9.4 GHz with a magnetic field modulation of 100 kHz for lock-in amplification using a conversion time of 164 ms, a time constant of 41 ms and a modulation amplitude of 0.2 mT. The microwave power was attenuated for each sample to record spectra under non-saturating conditions, typically 0.2 mW.
The magnetic field offset was corrected using 2,2-diphenyl-1-picryl-hydrazyl (Sigma-Aldrich, Buchs, Switzerland) and where necessary the cavity baseline was subtracted by measuring an empty or solvent-filled EPR capillary under the same conditions.
The spectra were processed and simulated using Matlab (The Mathworks, Natick, MA, USA) and EasySpin (7).

For *X-band parallel-mode EPR spectra*, samples (10 mM solution in toluene/cyclohexane 9:1) were transferred into 3 mm quartz capillaries (Wilmad-LabGlass, New Jersey, USA) in a glovebox, frozen in liquid nitrogen and flame-sealed on a Schlenk line under vacuum. Continuous-wave (cw) EPR spectra were recorded with a Bruker EMX spectrometer (Bruker Biospin, Rheinstetten, Germany) equipped with an ESR-900 Helium flow cryostat (Oxford Instruments, Oxfordshire, UK) and an ER-4116 dual mode cavity operating at ca. 9.35 GHz (parallel mode) with a magnetic field modulation of 100 kHz for lock-in amplification using a conversion time of 40 ms, a time constant of 10 ms, a modulation amplitude of 0.5 mT and a microwave power of 2 mW.

*$^{57}$Fe Mössbauer spectra* were recorded on powder samples contained in Delrin cups between 2.5 and 80 K on a low-field Mössbauer spectrometer equipped with a Janis SVT-400 cryostat or on a strong-field Mössbauer spectrometer equipped with an Oxford Instruments Spectromag 4000 cryostat containing an 8 T split-pair superconducting magnet. Both spectrometers were operated in a constant acceleration mode in transmission geometry. The isomer shifts were referenced against that of a room-temperature metallic iron foil. Analysis of the data was performed with the WMOSS Mössbauer Spectral Analysis Software (www.wmoss.org, 2012–2013, Web Research, Edina) and with a home-made program (SimuMoss software. C. Charavay, S. Segard, F. Edon, M. Clémancey, G. Blondin. CEA/iRTSV, CNRS, Univ. Grenoble Alpes) (8).

*SQUID magnetometry* was performed on a MPMS SQUID magnetometer (Quantum Design). A specific quartz glass sample holder was designed to perform magnetic measurements on air and moisture sensitive sample powder. All samples were prepared in a glove box ($O_2$<0.1 ppm, $H_2O$<0.1 ppm) under argon atmosphere after a careful calibration of the sample older: washing (HCl, ultra-pure water, $H_2SO_4/H_2O_2$, ultra-pure water, HCl, ultra-pure water, ethanol) and drying were followed by calibration and the holder was then filled with the sample powder and closed tightly. The weight of the measured sample (**3**) was 25.4 mg.

*NMR spectra* were recorded on a 300 MHz Bruker AVII spectrometer at room temperature. $^{1}H$ and $^{13}C$ spectra are reported in parts per million (ppm) and are calibrated with respect to the corresponding solvent residual peak. $^{13}C$ NMR spectra were recorded with complete proton decoupling and the spectra are likewise calibrated with respect to the corresponding solvent residual peak. Multiplet signals are reported as follows: s=singlet, d=doublet, t=triplet, q=quartet, quint=quintet, sept=septet, m=multiplet, b=broad, or combinations thereof.

*UV-Vis electronic absorption* data were collected on an Agilent Cary 60 UV-Vis Spectrophotometer, which was connected to a sampling probe (*d*=2 mm) inside the Glovebox with an optical fiber. Measurements were performed on $1.1 \cdot 10^{-4}$ M toluene solutions, unless stated otherwise. Spectral bands are classified as peaks (p) or shoulders (sh).

*Electrochemical data* were collected in a 20 mL or 5 mL cell, depending on convenience, using glassy carbon as working electrode (diameter 3 mm), a platinum wire as counter-electrode and a silver wire dipped in a 0.01 M solution of $AgNO_3$ in a 0.1 M solution of $[^{n}Bu_4N][PF_6]$ in MeCN as reference. The reference electrode was separated from the CV cell using a guard filled with the same electrolyte as used in the cell. The potential was controlled by a BioLogic SP-300 potentiostat. The mixture was stirred, and the working electrode polished after every scan.

*Elemental analyses* were carried out in the Mikrolabor of ETH Zürich on a LECO TruSpec® Micro spectrometer.

*Resonance Raman* spectra were recorded at room temperature on a Thermo Fischer DXR2 SmartRaman using 532 nm laser excitation and a 50 μm diameter pinhole on powdered samples. Samples were held in glass tubes sealed by a J. Young valve. The number of scans was adapted so to avoid sample fluorescence, but never decreasing below 64 scans. Additionally, samples were photobleached for 30 seconds prior to data collection.

Synthetic Procedures:

*2,2'',4,4'',6,6''-hexamethyl-1,1':3',1''-terphenyl-2'-thiol (DmpSH):* This compound was synthesized according to a modified in-house procedure.
In a dry three-necked 500 mL round-bottomed flask equipped with a reflux condenser and dropping funnel, Mg turnings (4.07 g, 167 mmol, 3.0 equiv.) were covered with 50 mL of dry THF. The dropping funnel was charged with pure bromomesitylene (24.4 mL, 167 mmol, 3.0 equiv.). A small amount of bromomesitylene was then added to the mixture, and the exothermic Grignard reaction was initiated upon gently warming the suspension with a heat gun. Subsequently, bromomesitylene was diluted in the dropping funnel with 80 mL of dry THF and added dropwise to the Mg turning suspension at a rate enabling to sustain the reflux of THF. After complete addition, the dark grey solution was heated at reflux for another 3 h, during which the Mg turnings dissolved entirely, before being let cool to room temperature. Meanwhile, in a dry two-necked 1 l round-bottomed flask, equipped with a dropping funnel and argon gas inlet, 2,6-dibromo-1-iodobenzene (20.07 g, 55.5 mmol, 1.0 equiv.) was dissolved in 150 mL dry THF. After cooldown, the MesMgBr solution prepared previously was transferred into the dropping funnel *via* PTFE cannula and dropwise added to the 2,6-dibromo-1-iodobenzene material over the course of 1 h. After additional 3 h at reflux, the mixture was cooled to –78°C (acetone/dry ice) and elemental sulfur (7.12 g, 222 mmol, 4.0 equiv.) was added as a solid, whereupon the color changed to a yellowish red. Stirring and warming to ambient temperature was continued for 2 days (*Note: For this reaction, elemental sulfur was used without prior sublimation for purification*). Afterwards, excess $S_8$ was filtered off by means of a frit and the solution was added to a slurry of $LiAlH_4$ (10.55 g, 278 mmol, 5.0 equiv.) in dry diethyl ether at 0°C. Stirring was subsequently continued for additional 2 days. Next, at 0°C, excess reducing agent was quenched using 75 mL of water, before the slurry was acidified by addition of 300 mL 10% aqueous HCl (*Note: evolution of toxic $H_2S$ gas; make sure the fume hood is ventilated properly!*). The aqueous phase was extracted with diethyl ether and the combined organic phases were dried over

$CaCl_2$ beads for several hours. The mixture was then filtered and the solution taken to dryness, yielding a pale yellow solid.
The crude product was recrystallized from hot EtOAc, affording DmpSH as off-white needle-shaped crystals (8.80 g, 46 %).
$^1$H NMR (300 MHz, Tol-d8): $\delta$ [ppm] 7.13 (s, 1H), 7.01 (s, 2H), 6.87 (s, 4H), 3.91 (s, 1H), 2.22 (s, 6H), 2.13 (s, 12H).
$^{13}$C NMR (75 MHz, Tol-d8): $\delta$ [ppm] 139.5, 137.9, 137.4, 136.3, 133.8, 128.9, 128.6, 125.4, 21.2, 20.2.

*[Fe(DmpS)$_2$]* was prepared by a modified literature procedure (9): A solution of [FeHMDS$_2$] (804.1 mg, 2.13 mmol, 1.0 equiv.) in toluene (10 mL) was added dropwise to a slurry of DmpSH (1.479 mg, 4.28 mmol, 2.0 equiv.) in pentane (30 mL). The reaction mixture immediately turned yellow, gradually changing to dark red over the course of 2 h. During this time a red, microcrystalline solid precipitated. The mixture was taken to dryness and the remaining red solid dissolved in a minimal amount of toluene. The dark red solution was layered with pentane and stored in a –30°C freezer. After 1 week, 1.02 g of red needle-shaped crystals were collected. Concentration of the supernatant, layering with pentane, followed by an additional recrystallization at –30°C afforded a second crop of 460 mg, yielding a total of 1.462 g (91.4 %) of product. The $^1$H NMR spectrum matches with previously reported data (9).
The identity of the product was further confirmed by X-ray diffraction analysis using a single crystal picked from the crystalized product prior to drying.
UV-Vis ($3.5\cdot10^{-4}$ M in Tol): $\lambda$ [nm] ($\varepsilon$ [$10^3$ $M^{-1}$ $cm^{-1}$]) 396 (p, 4.2), 448 (p, 6.1), 525 (sh, 1.7).
$^1$H NMR (300 MHz, $C_6D_6$): $\delta$ [ppm] 49.35 (s, 2H), 41.74 (s, 6H), 6.91 (s, 12H), –22.11 (bs, 4H), –24.56 (s, 1H).

*K[Fe(DmpS)$_2$]* (**1**)*:* Inside an argon-filled glovebox, in a cold-well submerged in a EtOAc/$N_2$ cooling mixture (approx. –90°C), a solution of [Fe(DmpS)$_2$] (1.292 g, 1.73 mmol, 1.0 equiv.) in toluene (20 mL) and $KC_8$ (241.0 mg, 1.78 mmol, 1.03 equiv.) were pre-cooled. Additionally, 4 Pasteur pipettes, a glass frit, pentane, toluene, and additional vials were pre-cooled in the cold-well or in the –30°C freezer, depending on convenience. $KC_8$ was slurried in a minimal amount of cold toluene and added to [Fe(DmpS)$_2$] using a cold Pasteur pipette, ensuring the complete transfer of reagents. The reaction mixture was then vigorously stirred while maintaining a low temperature over the course of 1 h. The color of the solution gradually changed from dark red to a dark greenish brown. After 20 minutes, the black graphite precipitate was removed by filtration and the solution was carefully layered with cold pentane before being stored at –30°C. After 5 days, 1.147 g (84 %) of product were collected as small dark brown needle-shaped crystals.
A single crystal suitable for X-ray diffraction analysis was grown by layering a dilute solution of the crude reaction mixture with cold pentane, followed by slow diffusion at –30°C over the course of 2 weeks. $^1$H NMR analysis in $C_6D_6$ and THF-d8 revealed that this compound is NMR silent.
UV-Vis ($3.8\cdot10^{-4}$ M in Tol): $\lambda$ [nm] ($\varepsilon$ [$10^3$ $M^{-1}$ $cm^{-1}$]) 356 (sh, 10.8), 421 (sh, 4.0), 483 (sh, 1.8), 568 (p, 0.6), 832 (p, 0.7).
Elemental analysis: ($C_{48}H_{50}FeS_2K$) expected: C 73.35 %, H 6.41 %; found: C 73.27 %, H 6.60 %.

*K$_2$[Fe$_2$S$_2$(DmpS)$_4$]* (**2**)*:* At –30°C, a solution of elemental sulfur, $S_8$ (2.5 mg, 0.078 mmol, 0.9 equiv.), in 3 mL of toluene was added to a solution of K[Fe(DmpS)$_2$] (68.8 mg, 0.088 mmol, 1.0 equiv.) in toluene under vigorous stirring. The color changed immediately from dark green to dark yellowish brown. Stirring was continued for 2 days at room temperature. The reaction mixture was then taken to dryness and the resulting dark brown solid was washed with pentane, dried and dissolved in a mixture of diethyl ether and HMDSO (1:1). A dark precipitate was centrifuged off and the supernatant was set for crystallization by slow evaporation of diethyl ether into a HMDSO phase. After 1 week, 10.7 mg (15 %) of product were isolated as black block-shaped crystals. A single-crystal suitable for X-ray diffraction analysis was picked from the purified product prior to drying. No $^1$H NMR signals could be observed in $C_6D_6$.
UV-Vis ($2.3\cdot10^{-4}$ M in Tol): $\lambda$ [nm] ($\varepsilon$ [$10^3$ $M^{-1}$ $cm^{-1}$]) 334 (sh, 20.2), 416 (sh, 7.2).

*K$_2$[Fe$_4$S$_4$(DmpS)$_4$]* (**5**)*:* A solution of elemental sulfur, $S_8$ (216.9 mg, 6.77 mmol, 2.0 equiv.), in toluene (25 mL) and K[Fe(DmpS)$_2$] (2.672 g, 3.39 mmol, 1.0 equiv.), which was added as solid were successively added to a slurry of [Fe(DmpS)(TripS)] (2.165 g, 1.70 mmol, 0.5 equiv.) in toluene (120 mL). The reaction mixture immediately turned to a homogeneous solution of yellowish dark brown color and stirring was continued for 3 days at room temperature. The solvent was removed in vacuo, and the remaining solid was slurried with pentane and taken to dryness to remove traces of toluene. The crude product was extracted into a 5:1 mixture of diethyl ether (100 mL) and HMDSO (20 mL), from which pale-yellow by-products were removed by filtration. Purification was carried out by slow

Schlenk-to-Schlenk evaporation of diethyl ether from the mother liquor into a pure HMDSO phase (50 mL) *via* U-shaped glass connection. After 3 weeks, the product, $K_2[Fe_4S_4(DmpS)_4]$, was collected as large black hexagonal plate-shaped crystals, which were washed with pentane and dried in *vacuo* (2.220 g, 69 %).
Such single crystals, grown by slow evaporation of diethyl ether from an $Et_2O$/HMDSO mixture, were measured by XRD several times. However, while data quality was sufficient to establish the identity as $K_2[Fe_4S_4(DmpS)_4]\cdot Et_2O\cdot$HMDSO, the structure data was not deemed of sufficient quality for the purposes of this study. This was attributable to the large volume of the corresponding unit cell.
Single crystals better suitable for X-ray diffraction analysis were grown by layering HMDSO with a solution of the product in diisopropyl ether and allowing for slow diffusion at room temperature.
UV-Vis ($1.1\cdot10^{-4}$ M in Tol): $\lambda$ [nm] ($\varepsilon$ [$10^3$ $M^{-1}$ $cm^{-1}$]) 340 (p, 19.9), 404 (p, 22.8).
$^1$H NMR (300 MHz, $C_6D_6$): $\delta$ [ppm] 8.26 (d, $J^4$=7.1 Hz, 2H), 7.09 (s, 4H), 6.36 (bs, 1H), 2.55 (s, 12H), 2.48 (s, 6H).
$^1$H NMR (300 MHz, THF-d8): $\delta$ [ppm] 8.06 (d, $J^4$=7.0 Hz, 2H), 6.87 (s, 4H), 6.10 (1s, H), 2.24 (s, 6H), 2.18 (s, 12H).
$^{13}$C NMR (75 MHz, $C_6D_6$): $\delta$ [ppm] 141.4, 139.9, 136.3, 132.1, 130.1, 129.4, 30.3, 21.5.
$^{13}$C NMR (75 MHz, THF-d8): $\delta$ [ppm] 142.2, 140.7, 136.9, 132.0, 130.8, 129.8, 31.0, 22.5.
Elemental analysis: ($C_{96}H_{100}Fe_4S_8K_2\cdot C_4H_{10}O$) expected: C 63.68 %, H 5.88 %; found: C 63.38 %, H 5.89 %.

*$K_4[Fe_4S_4(DmpS)_4]$* (**3**)*:* A slurry of $KC_8$ (82.1 mg, 0.607 mmol, 2.2 equiv.) in toluene was added to a solution of $K_2[Fe_4S_4(DmpS)_4]$ (501.6 mg, 0.277 mmol, 1.0 equiv.). The resulting suspension was stirred for 1 h before the black graphite precipitate was removed by centrifugation. The dark red toluene solution was layered with an equivalent volume of HMDSO and stored at room temperature overnight. After 3 days, $K_4[Fe_4S_4(DmpS)_4]$, was collected as large black needle-shaped crystals, which were washed with pentane and dried in *vacuo*, affording 471.6 mg (90 %) of product.
Large single crystals suitable for X-ray diffraction analysis were grown analogously, from a more dilute toluene solution. For elemental analysis, the sample was mortared and dried in high vacuum (approx. $10^{-6}$ mbar).
UV-Vis ($1.1\cdot10^{-4}$ M in Tol): $\lambda$ [nm] ($\varepsilon$ [$10^3$ $M^{-1}$ $cm^{-1}$]) 347 (sh, 18.9), 520 (sh, 4.0).
$^1$H NMR (300 MHz, $C_6D_6$): $\delta$ [ppm] 26.81 (bs), 2.64 (bs), –15.30 (bs).
Elemental analysis: ($C_{96}H_{100}Fe_4S_8K_4\cdot 0.4C_6H_{18}Si_2O$) expected: C 60.45 %, H 5.53 %; found: C 60.49 %, H 5.36 %.

*$K_3[Fe_4S_4(DmpS)_4]$* (**4**)*:* $K_2[Fe_4S_4(DmpS)_4]$ (80.3 mg, 0.0392 mmol, 1.0 equiv.) and $K_4[Fe_4S_4(DmpS)_4]$ (86.5 mg, 0.0391 mmol, 1.0 equiv.), each dissolved in 7 mL of toluene, were mixed in a 20 mL scintillation vial at room temperature. The dark brown solution was stirred for 3 h, before being concentrated to about half of the original volume, centrifuged and overlayered with HMDSO. After 4 days, dark needle-shaped crystals were collected, which were washed with pentane and dried in *vacuo*, affording 130.2 mg (77 %) of product.
Single crystals suitable for X-ray diffraction analysis were grown analogously, form a more dilute toluene solution.
UV-Vis ($1.1\cdot10^{-4}$ M in Tol): $\lambda$ [nm] ($\varepsilon$ [$10^3$ $M^{-1}$ $cm^{-1}$]) 347 (sh, 19.2), 416 (sh, 14.4).
$^1$H NMR (300 MHz, $C_6D_6$): $\delta$ [ppm] 10.41 (bs), 8.15 (bs), 6.26 (bs), 2.97-2.22 (m).
Elemental analysis: ($C_{96}H_{100}Fe_4S_8K_4\cdot 2C_6H_{18}Si_2O$) expected: C 59.62 %, H 6.30 %; found: C 59.57 %, H 6.22 %.

*$K[Fe_4S_4(DmpS)_4]$* (**6**)*:* Under vigorous stirring, a toluene solution (10 mL) of $K_2[Fe_4S_4(DmpS)_4]$ (150 mg, 0.0828 mmol, 1.0 equiv.) was added to ferrocenium hexafluorophosphate (31.3 mg, 0.0948 mmol, 1.1 equiv.) in a 20 mL scintillation vial. Stirring was continued for 3 h, during which the color changed from dark yellowish brown to dark purple. The mixture was filtered and concentrated to approximately 2 mL. It was then filtered again and layered with HMDSO at room temperature. After 4 days of slow diffusion, black crystals of $K[Fe_4S_4(DmpS)_4]$ were decanted, washed with pentane and dried, affording 79.7 mg (59 %) of product.
Single crystals suitable for X-ray diffraction analysis were grown analogously, from a more dilute toluene solution.
UV-Vis ($1.1\cdot10^{-4}$ M in Tol): $\lambda$ [nm] ($\varepsilon$ [$10^3$ $M^{-1}$ $cm^{-1}$]) 347 (sh, 20.4), 469 (p, 26.7).
$^1$H NMR (300 MHz, $C_6D_6$): $\delta$ [ppm] 10.01 (d, $J$=7.4 Hz, 2H), 6.84 (s, 4H), 4.26 (t, $J$=7.3 Hz, 1H), 2.79 (s, 12H), 2.59 (s, 6H).
Elemental analysis: ($C_{96}H_{100}Fe_4S_8K\cdot C_7H_8$) expected: C 66.49 %, H 5.84 %; found: C 66.26 %, H 5.86 %.

*$[Fe_4S_4(DmpS)_4]$* (**7**)*:* Under vigorous stirring, ferrocenium hexafluorophosphate (106.2 mg, 0.321 mmol, 2.2 equiv.) was added to a toluene solution (10 mL) of $K_2[Fe_4S_4(DmpS)_4]$ (300 mg, 0.146 mmol, 1.0 equiv.) in a 20 mL scintillation vial. Stirring was continued for 5 h, during which the color changed from dark yellowish brown to dark blue. The mixture was filtered and taken to dryness. It was then rapidly slurried with pentane and dried another time

in order to remove trace amounts of toluene. The crude product was washed with hot HMDSO (3x30 ml) and dried in high-vacuum ($10^{-6}$ mbar) for two days, yielding 168.1 mg (61 %) of product as black powder.
Single crystals suitable for X-ray diffraction analysis were grown from a dilute hot HMDSO solution of product upon undisturbed standing at room temperature for 1 week.
UV-Vis ($1.1 \cdot 10^{-4}$ M in Tol): $\lambda$ [nm] ($\varepsilon$ [$10^3$ $M^{-1}$ $cm^{-1}$]) 341 (sh, 20.2), 521 (p, 35.8).
$^1$H NMR (300 MHz, $C_6D_6$): $\delta$ [ppm] 10.75 (d, *J*=7.4 Hz, 2H), 7.13 (s, 4H), 3.44 (t, *J*=6.1 Hz, 1H), 2.79 (s, 12H), 2.74 (s, 6H).
$^{13}$C NMR (75 MHz, $C_6D_6$): $\delta$ [ppm] 149.0, 145.5, 141.1, 136.8, 129.1, 127.9, 124.4, 26.3, 21.2.
Elemental analysis: ($C_{96}H_{100}Fe_4S_8 \cdot C_6H_{18}Si_2O$) expected: C 64.61 %, H 6.27 %; found: C 64.54 %, H 6.23 %.

**Supplementary Text**

Synthesis and Characterization of **1**

Intrigued by the fact that the $[Fe_4S_4]^0/[Fe_4S_4]^{1+}$ redox wave of $[Fe_4S_4(SPh)_4]^{2-}$ could only be observed quasi-reversibly in Pickett's non-coordinating eutectic electrolyte (10), we investigated the chemistry of low-valent iron complexes bearing bulky terphenyl thiolates as supporting ligands, which are capable of engaging in metal-arene interactions. These compounds, originally devised by Power and co-workers in the 90's, are readily soluble in non-polar solvents – even as alkaline metal salts (11, 12) – but their electrochemistry remains largely unexplored. Bearing in mind that metal-arene backbonding interactions are capable of stabilizing low oxidation states, and steric bulk in general increases the donor strength of a ligand, $[Fe(DmpS)_2]$ (where DmpS is 2,2'',4,4'',6,6''-hexamethyl-1,1':3',1''-terphenyl-2'-thiolate) was envisioned to have a particularly rich redox chemistry (9). In fact, we found that reduction of $[Fe(DmpS)_2]$ over potassium graphite at –90°C in toluene afforded $K[Fe(DmpS)_2]$ (**1**), a rare example of a pseudo homoleptic $Fe^{I}$-thiolate complex, for which, to the best of our knowledge, the only known similar example is Holland's *bis*(thiolate) supported chelate with a phenyl anchor motif (13). The anionic $Fe^{I}$-complex retains its solubility in toluene even as potassium-salt, due to interaction of the $K^+$-ion with one of the mesitylene substituents and adjacent thiolates. Accordingly, the cyclic voltammogram of $[Fe(DmpS)_2]$ in {$[^nBu_4N][BF_4]$·3 toluene} exhibits a reversible redox wave at –1.88 V (Fig. S2) and a second redox event at –0.02 V. Slow diffusion of pentane into a layer of **1** in toluene at –30°C afforded single crystals suitable for X-ray diffraction analysis. Compound **1** was found to crystallize as a coordination polymer in the space group $P2_1/c$ with a single molecule of **1** in the asymmetric unit. Upon reduction, the perpendicular mesitylene-Fe distance decreases from 2.458(2) and 2.431(2) Å (av. 2.445(2) Å) in $[Fe(DmpS)_2]$ to 1.547(1) Å in **1** ($Fe–C^{mes}$ 2.041(3)-2.133(3) Å), indicative of significant iron-arene back-bonding (Fig. S30). A frozen toluene solution of **1** exhibits a rhombic EPR spectrum with principal *g*-values of 2.188, 2.029 and 1.993 (Fig. S22), which suggests a low-spin $Fe^{I}$, $d^7$, $S$=1/2 spin system and is in line with the data reported for Holland's complex (13).

Redox Transformations of **5**:

Firstly, twofold chemical reduction of dark yellowish-brown cluster **5** over a small excess of potassium graphite at room temperature yields all-ferrous dark red $K_4[Fe_4S_4(DmpS)_4]$ (**3**). **3** crystallizes from a toluene solution layered with HMDSO at room temperature in the space group $P\bar{4}2_1c$ (No. 114) and its solid-state molecular structure is shown in Fig. 2*A* & S41. Notably, the UV-Vis absorption spectrum of **3** shows a continuous rise towards higher energy with a prominent shoulder at 520 nm (Fig. 4*D*). **3** is stable in toluene and THF as solvents, but decomposes rapidly in MeCN solution, as evidenced by UV-Vis spectroscopy (Fig. S10).
A stoichiometric comproportionation of **3** and **5** was then used to synthesize $K_3[Fe_4S_4(DmpS)_4]$ (**4**), the singly reduced analogue of **5**. **4** also crystallizes in the space group $P\bar{4}2_1c$ (No. 114), but possesses a disordered K-vacancy, resulting in a site-occupancy of 0.75 (refines *free* to 0.747(9)) for the K-ion. The corresponding structure can be viewed in Fig. 2*B* and S34. Furthermore, a redox titration experiment monitored by UV-Vis electronic absorption spectroscopy confirms the clean, isosbestic conversion of **3** and **5**, forming the new species, **4**, upon comproportionation (Fig. 4*D*) (14). Note that the similarity of the space group of **3** and **4**, as well as the fact that the $[Fe_4S_4]^{1+/2+}$ and $[Fe_4S_4]^{0/1+}$ redox couples lie close in potential (Fig. S6 & S7), poses a significant risk for co-crystallization, thereby contaminating **4** with **3**. While redox transformations toward forming **4** can be carried out with single equivalents of reagents ($KC_8$ or $FcPF_6$, respectively), starting from either **5** or **3,** we opted for the route using comproportionation, because it enables weighing-in compounds with higher accuracy and, thus, minimizes the risk of redox impurity in **4**.
Treatment of **5** with a small excess of ferrocenium hexafluorophosphate in toluene generates dark purple colored $K[Fe_4S_4(DmpS)_4]$ (**6**), the singly-oxidized analogue of **5**, which crystalizes in space group $P\bar{1}$ (No. 2). Its solid-state molecular structure is shown in Fig. 2*D* & S35. In line with previous reports on molecular models and biological samples, **6** shows electronic absorption bands centered at 347 and 469 nm (Fig. 4*D*). The CV data recorded on **5** and **6** in THF containing 0.3 M $[^nBu_4N][PF_6]$ as electrolyte and {$[^nBu_4N][BF_4]$·3 toluene}, respectively (Fig. S3-S5), matches the data measured for $[Fe_4S_4(DmpS)_4]^-$ in ref. (15). Note that a comparison of the voltammograms of **5** and **6** enables a straightforward assignment of redox events, because the open-circuit potential changes from the cathodic to the anodic side of the redox wave at –0.85 V, confirming its assignment to the $[Fe_4S_4]^{2+/3+}$ couple (Fig. S3 & S4, respectively ; open-circuit potential indicated with *black arrows*). Such a cathodic shift of the redox

potentials of synthetic clusters with respect to protein-bound analogues is common and likely originates from the much poorer solvation of anionic species in aprotic organic media *versus* aqueous ones (14-16).
Last, 2.2 equivalents of ferrocenium hexafluorophosphate were used to generate dark blue all-ferric $[Fe_4S_4(DmpS)_4]$ (**7**), crystals of which could be isolated from a hot HMDSO solution upon prolonged standing. It crystalizes in space group $P2_12_12_1$ (No. 19) and its solid-state molecular structure is shown in Fig. 2*E* and S36. $^1H$ and $^{13}C$ NMR spectroscopy revealed all signals of the $DmpS^-$ ligand present in the diamagnetic region of the spectrum (Fig. S20 & S21), similar to what has been reported for $[Fe_4S_4(TbtS)_4]$, which is, to the best of our knowledge, the only other literature-known all-ferric iron-sulfur cubane (17). **7** exhibits an intense broad electronic absorption band at 521 nm, completing the trend of isosbestic increase in extinction upon oxidation from **3**-**7**. Although no evidence has been reported that this oxidation state is accessible in biological media, it is the last member of the $[Fe_4S_4]$ electron transfer series, accessible by 1-electron transformation of the individual Fe-atoms.
The chemical reversibility of the $[Fe_4S_4]^{0/1+}$ redox couple was separately confirmed by monitoring the stoichiometric reduction of **4** to **3** using $KC_8$, followed by the oxidation of **3** to **4** using $FcPF_6$ with UV-Vis spectroscopy (Fig. S11). Each member of the redox series **3**-**7** has a distinct spectroscopic signature. The purity of the individual compounds was therefore established by the spectroscopic methods presented herein as well as CH combustion analysis multiple times and on independently synthesized samples.

**Supplementary Figures and Tables**

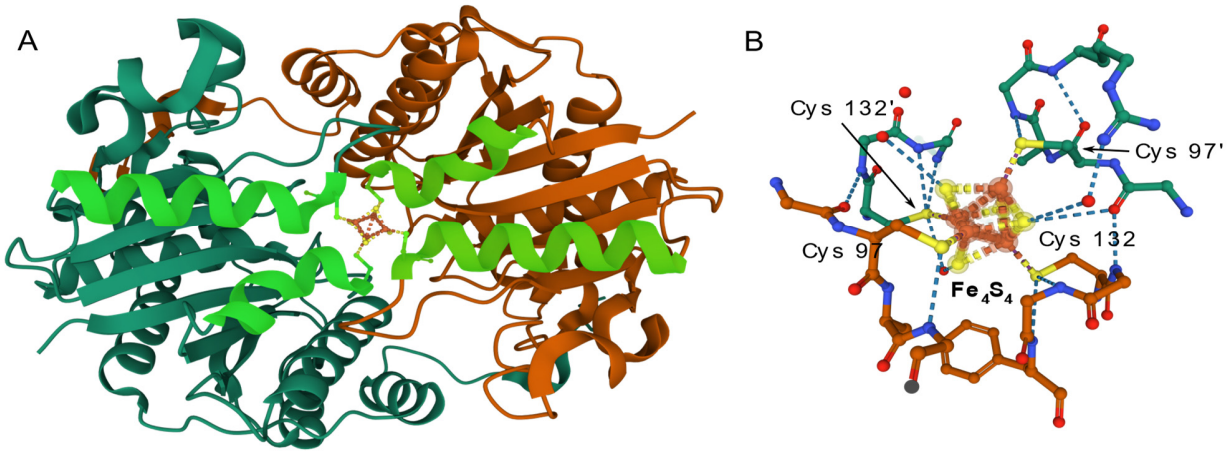


**Figure S1.**
Biological structure data 1G1M (18) visualized with Mol* Viewer (19), and highlighting interactions, which stabilize reduced states of the $Fe_4S_4$ cofactor. (*A*) Ribbons representation of the 1G1M FeP structure. $\alpha$- and $\beta$-subunits of the homodimer are represented in *green* and *orange*, respectively. The four $\alpha$-helices surrounding the $Fe_4S_4$ cofactor are highlighted in *light green* color. (*B*) Detailed coordination environment (5 Å radius) of the $Fe_4S_4$ core. Possible hydrogen bonding interactions are highlighted by dashed *blue* lines.

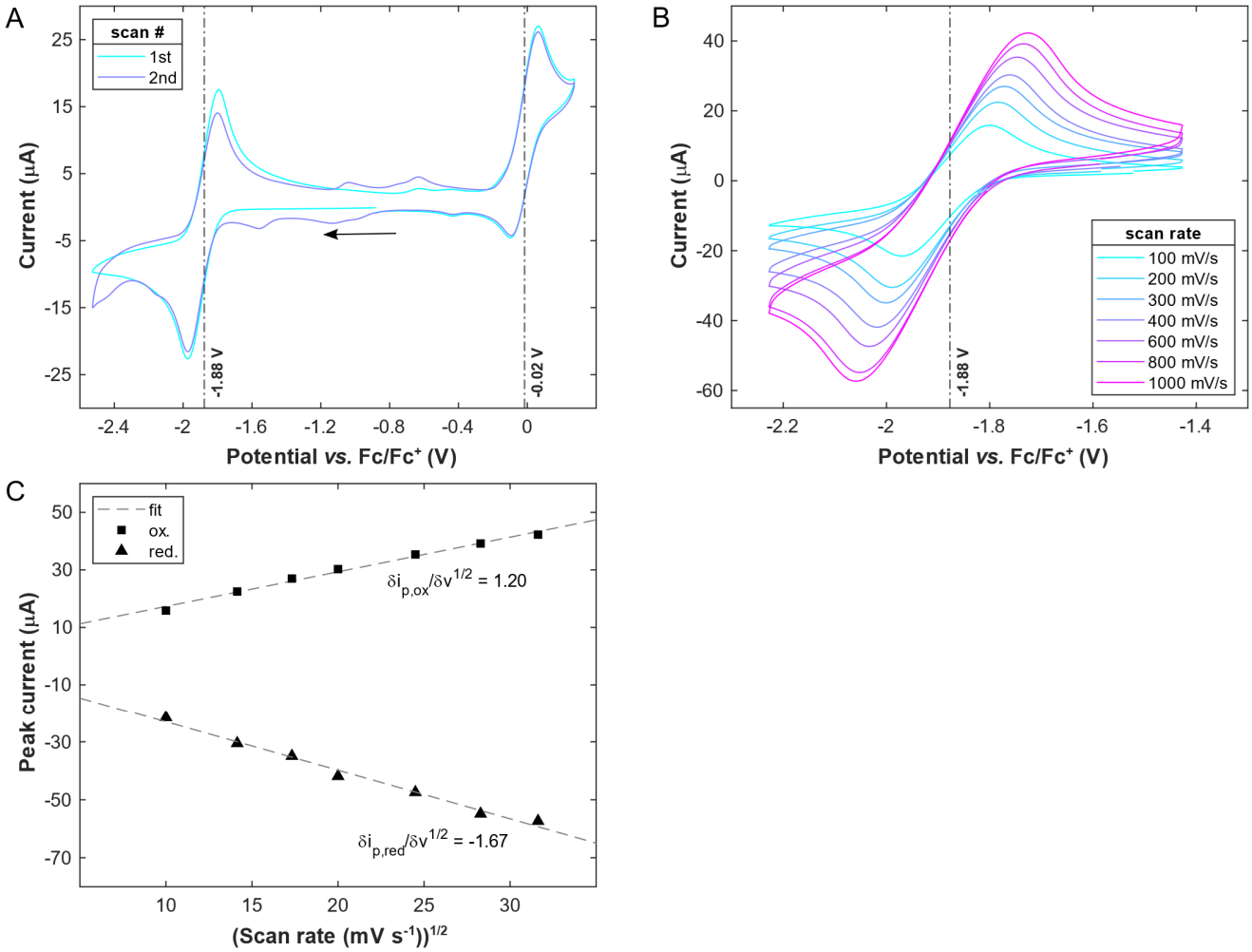


**Figure S2.**
Electrochemical data for [Fe(DmpS)$_2$] recorded on a 7 mM solution of complex in {[$^n$Bu$_4$N][BF$_4$]·3 toluene} electrolyte. (*A*) Cyclic voltammogram recorded with a scan rate of 100 mV s$^{-1}$ using a glassy carbon working-electrode, Ag/AgNO$_3$ reference-electrode and platinum wire as counter-electrode. Subsequent scans are shown in shades of blue and potentials are referenced against the Fc/Fc$^+$ couple. (*B*) Reversible reduction wave of the [Fe$^{II}$(DmpS)$_2$]/[Fe$^{I}$(DmpS)$_2$] redox couple recorded at different scan rates. (*C*) Peak current, $i_p$, plotted against the square root of the scan rate, *v*.

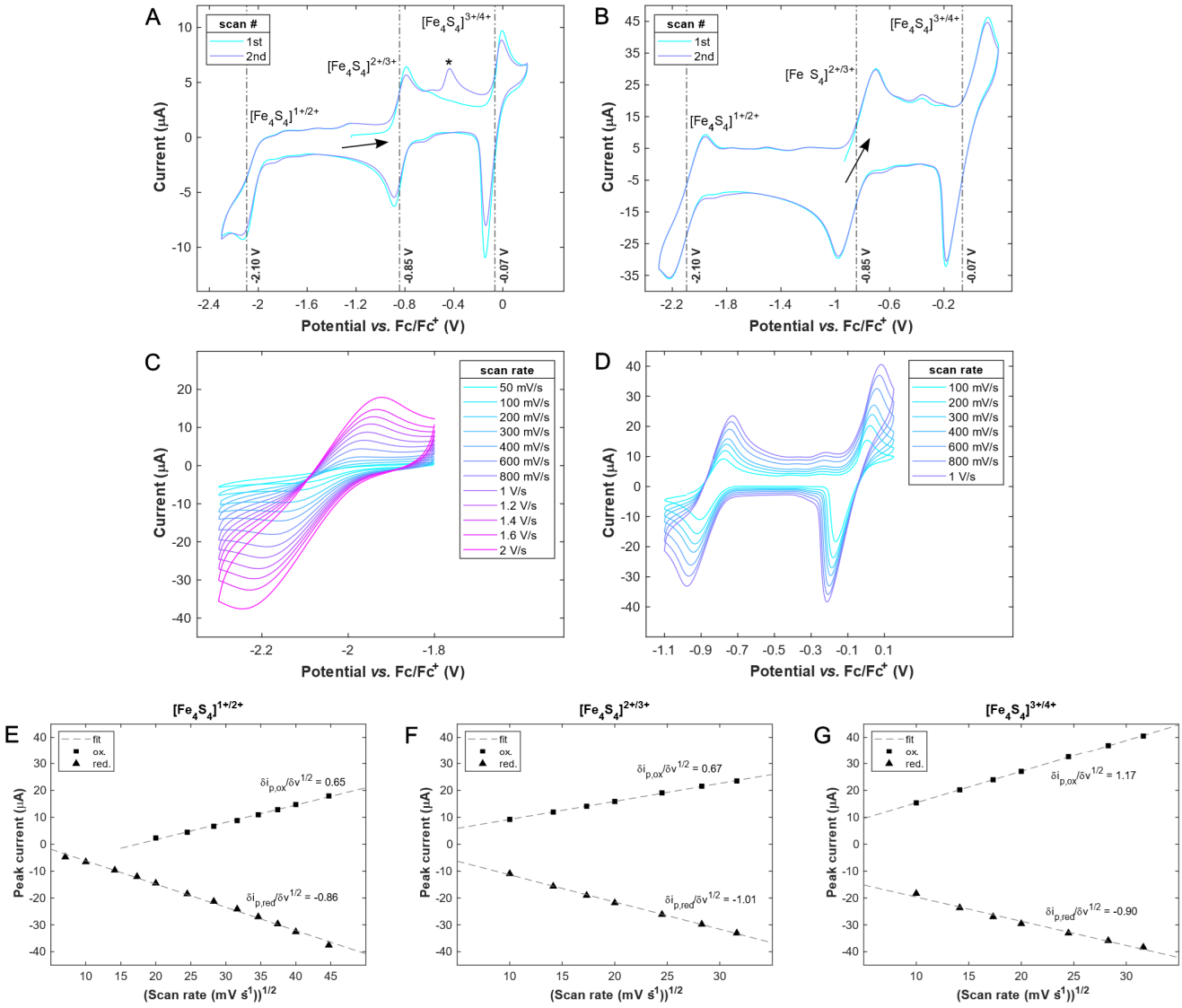


**Figure S3.**
Electrochemical data for **5** recorded on a 3 mM solution of the cluster in {[$^n$Bu$_4$N][BF$_4$]·3 toluene} electrolyte. (*A*) Cyclic voltammogram recorded with a scan rate of 100 mV s$^{-1}$ using a glassy carbon working-electrode, Ag/AgNO$_3$ reference-electrode and platinum wire as counter-electrode. Subsequent scans are shown in shades of blue and potentials are referenced against the Fc/Fc$^+$ couple. The impurity signal marked by an asterisk only appears after scanning the [Fe$_4$S$_4$]$^{1+/2+}$ couple. (*B*) Cyclic voltammogram recorded with a scan rate of 1000 mV s$^{-1}$. (*C*, *D*) Redox events corresponding to [Fe$_4$S$_4$]$^{1+/2+}$ (*C*), and [Fe$_4$S$_4$]$^{2+/3+}$ and [Fe$_4$S$_4$]$^{3+/4+}$ (*D*), respectively, recorded at different scan rates. (*E*-*G*) Peak current, $I_p$, plotted against the square root of the scan rate, $v$, for all three redox-couples.

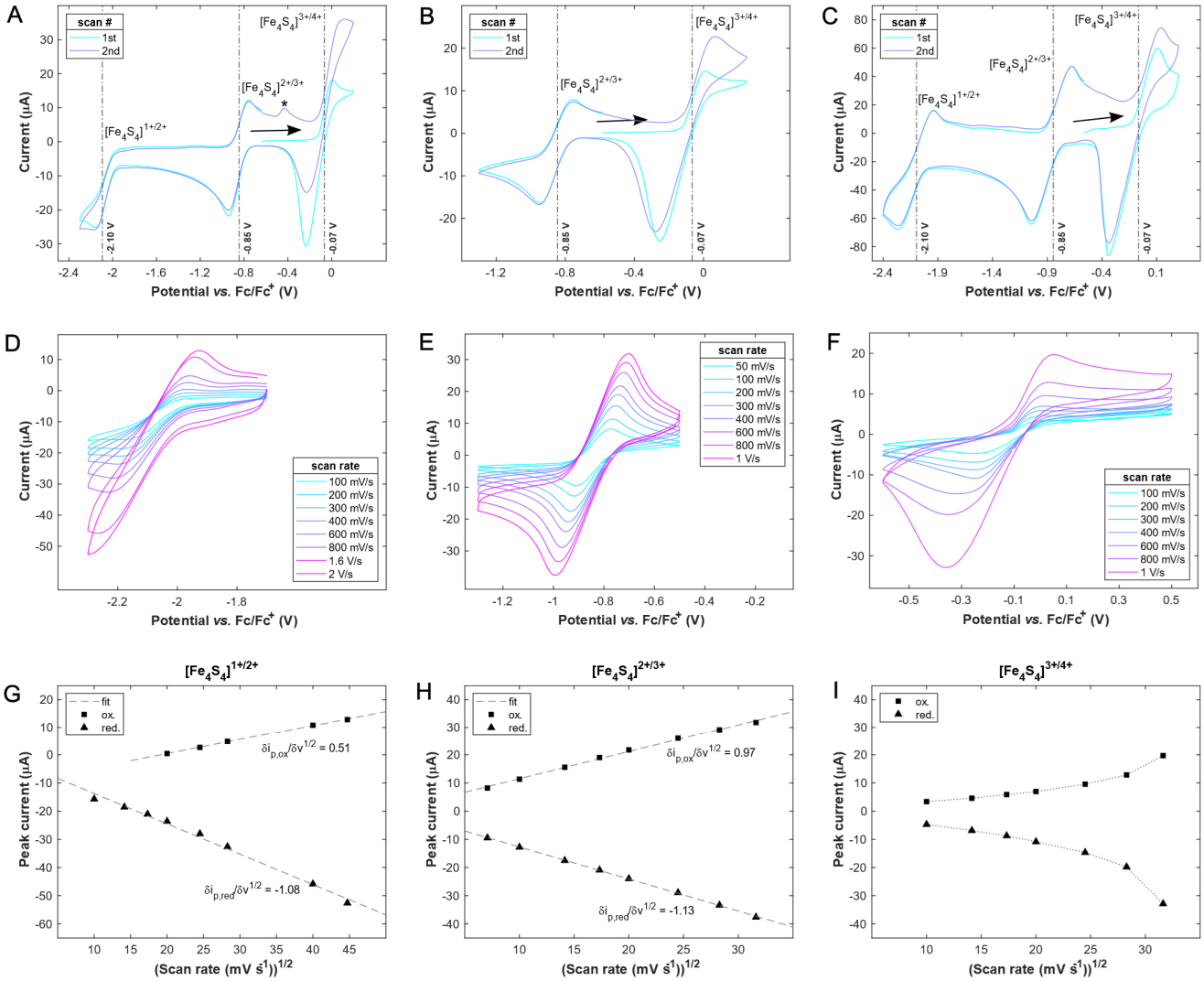


**Figure S4.**
Electrochemical data for **6** recorded on a 5 mM solution of the cluster in {[$^n$Bu$_4$N][BF$_4$]·3 toluene} electrolyte. (*A*) Cyclic voltammogram recorded with a scan rate of 100 mV s$^{-1}$ using a glassy carbon working-electrode, Ag/AgNO$_3$ reference-electrode and platinum wire as counter-electrode. Subsequent scans are shown in shades of blue and potentials are referenced against the Fc/Fc$^+$ couple. The impurity signal marked by an asterisk only appears after scanning the [Fe$_4$S$_4$]$^{1+/2+}$ couple. (*B*) Cyclic voltammogram of the [Fe$_4$S$_4$]$^{2+/3+}$ and [Fe$_4$S$_4$]$^{3+/4+}$ redox couples recorded with a scan rate of 100 mV s$^{-1}$. (*C*) Cyclic voltammogram recorded with a scan rate of 2000 mV s$^{-1}$. (*D-F*) Redox events corresponding to [Fe$_4$S$_4$]$^{1+/2+}$ (*D*), [Fe$_4$S$_4$]$^{2+/3+}$ (*E*) and [Fe$_4$S$_4$]$^{3+/4+}$ (*F*), respectively, recorded at varying scan rates. (*G-I*) Peak current, $I_p$, plotted against the square root of the scan rate, *v*, for all three redox-couples.

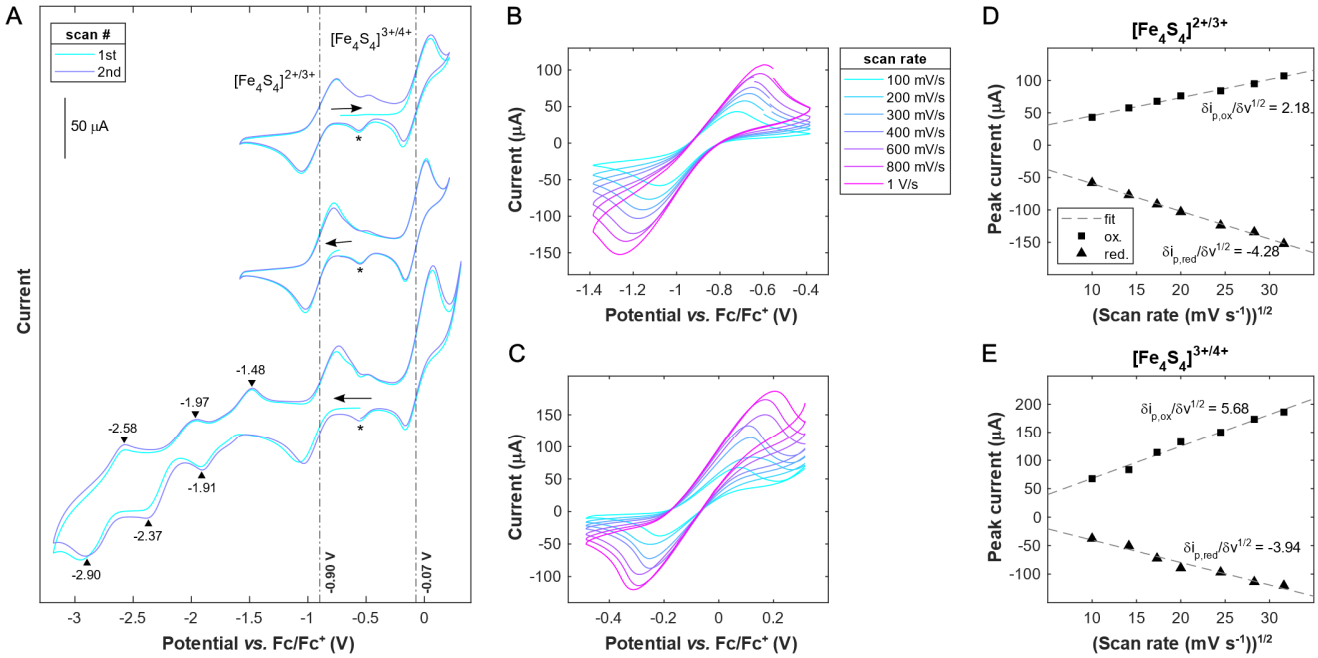


**Figure S5.**
Electrochemical data of **6** recorded on a 7 mM solution of cluster in 0.3 M [$^n$Bu$_4$N][PF$_6$] in THF. (*A*) Cyclic voltammograms of **6** recorded with a scan rate of 50 mV s$^{-1}$ using a glassy carbon working-electrode, Ag/AgNO$_3$ reference-electrode and platinum wire as counter-electrode. Subsequent scans are shown in shades of blue and potentials are referenced versus the Fc/Fc$^+$ couple. The impurity signal marked by an asterisk only appears after scanning the [Fe$_4$S$_4$]$^{3+/4+}$ couple and is caused by dissociation of a thiolate ligand, as reported in (20). (*B*,*C*) Cyclic voltammogram of the [Fe$_4$S$_4$]$^{2+/3+}$ (*B*) and [Fe$_4$S$_4$]$^{3+/4+}$ (C) redox couples recorded at varying scan rates. (*D*,*E*) Peak current, $I_p$, plotted against the square root of the scan rate, $v$, for both redox-couples.

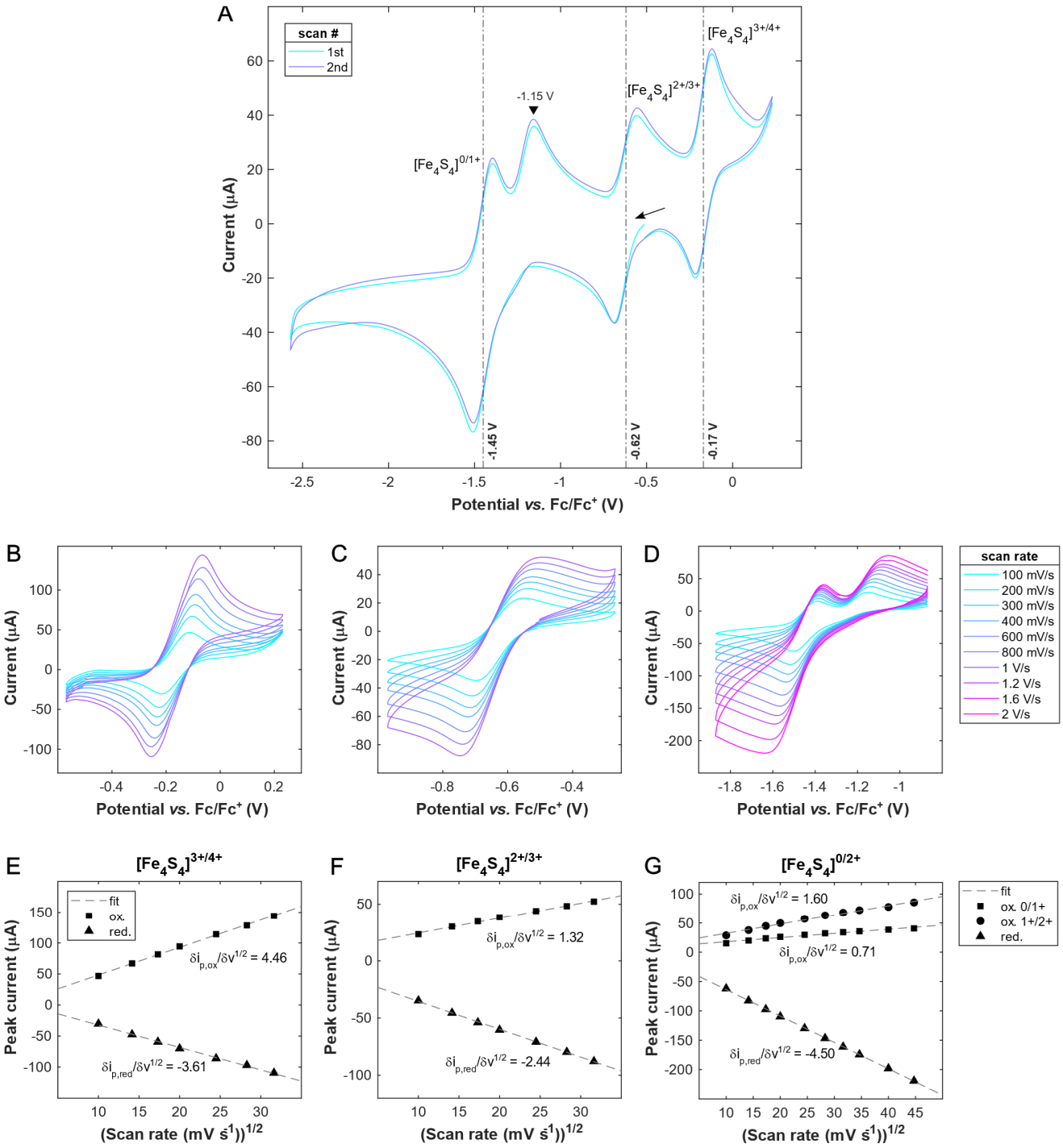


**Figure S6.**
Electrochemical data of **6** recorded on a 6 mM solution of cluster in 0.3 M K[BArF$_{24}$] in THF. (*A*) Cyclic voltammogram of **6** recorded with a scan rate of 100 mV s$^{-1}$ using a glassy carbon working-electrode, Ag/AgNO$_3$ reference-electrode and platinum wire as counter-electrode. Subsequent scans are shown in shades of blue and potentials are referenced versus the Fc/Fc$^+$ couple. (*B-D*) Cyclic voltammogram of the $[Fe_4S_4]^{3+/4+}$ (*B*), $[Fe_4S_4]^{2+/3+}$ (*C*) and $[Fe_4S_4]^{0/1+/2+}$ (*D*) redox couples recorded at varying scan rates. (*E-G*) Peak current, $I_p$, plotted against the square root of the scan rate, *v*, for all four redox-couples.

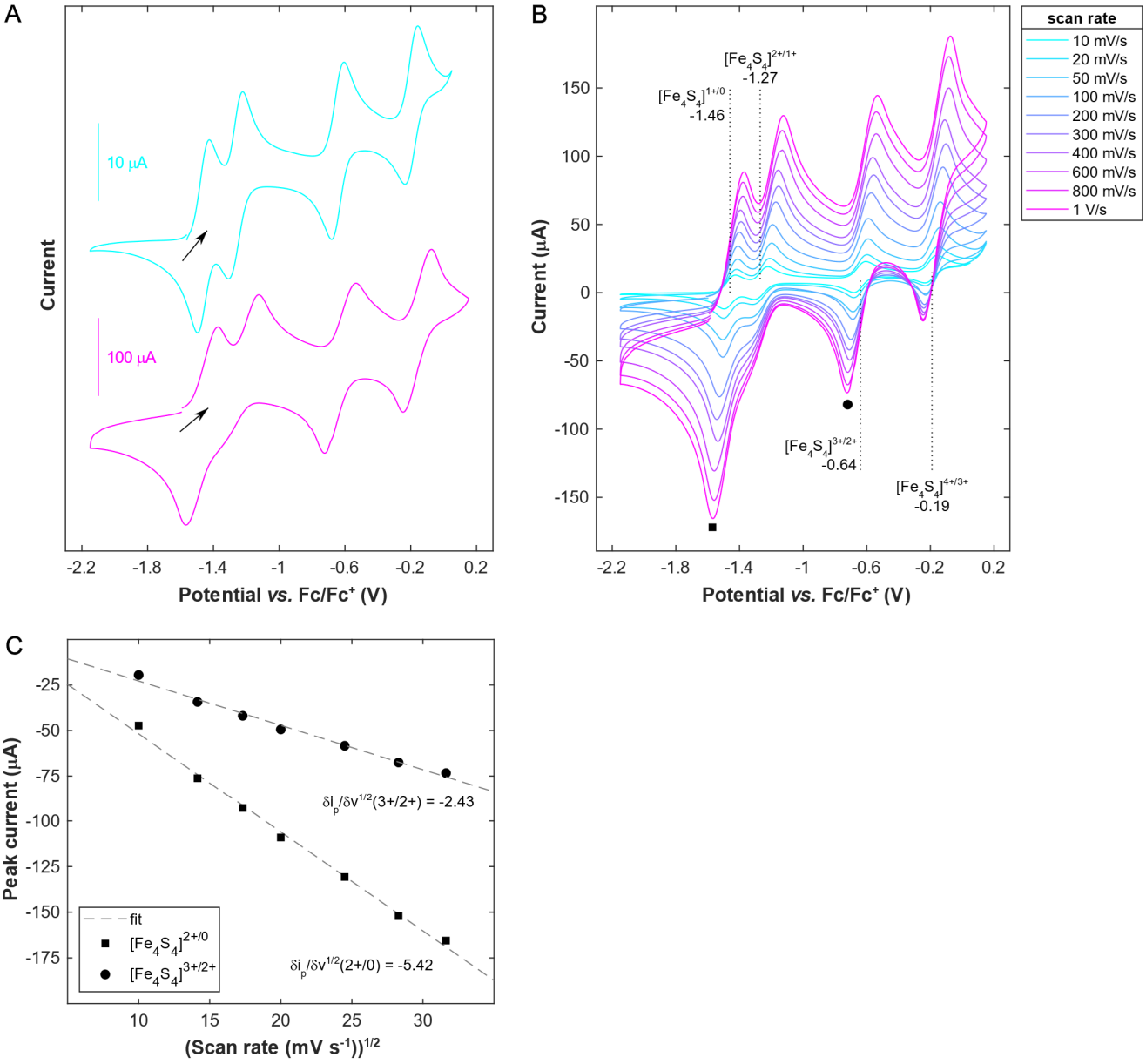


**Figure S7.**
Electrochemical data of **3** recorded on a 5 mM solution of cluster in 0.3 M K[$BArF_{24}$] in THF. (*A*) Cyclic voltammogram of **3** recorded with scan rates of 10 mV $s^{-1}$ (*cyan*) and 1 V $s^{-1}$ (*magenta*), respectively, using a glassy carbon working-electrode, $Ag/AgNO_3$ reference-electrode and platinum wire as counter-electrode. Potentials are referenced versus the $Fc/Fc^+$ couple. (*B*) Cyclic voltammogram of **3** recorded at varying scan rates. (*C*) Peak current, $I_p$, plotted against the square root of the scan rate, *v*, for the reductive peak current responses of the $[Fe_4S_4]^{3+/2+}$ (*black circles*) and $[Fe_4S_4]^{2+/0}$ (*black squares*) redox couples.

**Table S1.**
Summary of half-wave-potentials for the redox couples of the redox series **3**-**7** as determined by cyclic voltammetry in THF solution, using [$^{n}$Bu$_4$N][PF$_6$] or K[BArF$_{24}$] as electrolyte salt and in {[$^{n}$Bu$_4$N][PF$_6$]·3 toluene}

| **electrolyte** | {[$^{n}$Bu$_4$N][BF$_4$]·3 toluene} | THF / [$^{n}$Bu$_4$N][PF$_6$] | THF / K[BArF$_{24}$] |
|---|---|---|---|
| $E_{1/2}([Fe_4S_4]^{3+/4+})$ (**6**/**7**) | -0.07 V | -0.06 V | -0.19 V |
| $E_{1/2}([Fe_4S_4]^{2+/3+})$ (**5**/**6**) | -0.85 V | -0.90 V | -0.64 V |
| $E_{1/2}([Fe_4S_4]^{1+/2+})$ (**4**/**5**) | -2.10 V | - | -1.27 V |
| $E_{1/2}([Fe_4S_4]^{0/1+})$ (**3**/**4**) | - | - | -1.46 V |

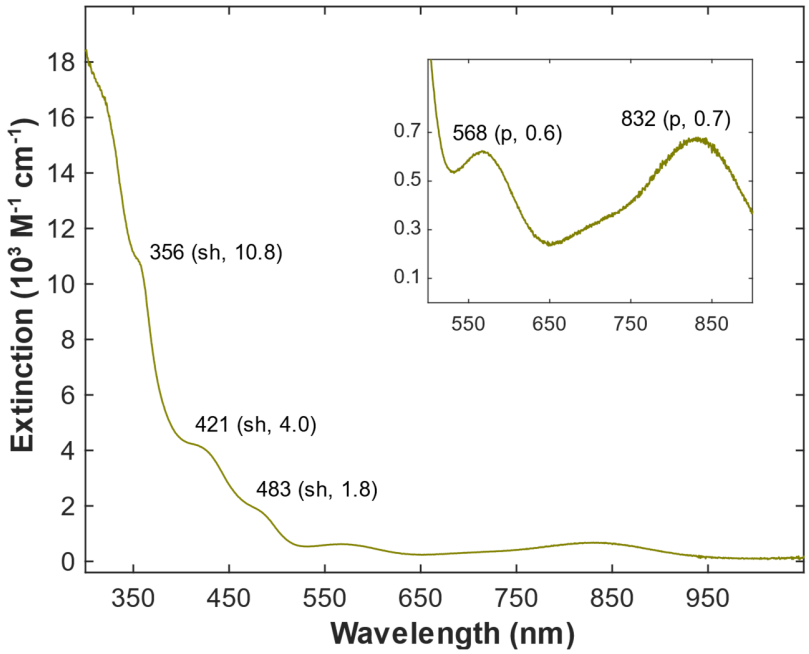


**Figure S8.**
UV-Vis electronic absorption spectrum of a $3.8 \cdot 10^{-4}$ M toluene solution of **1**.

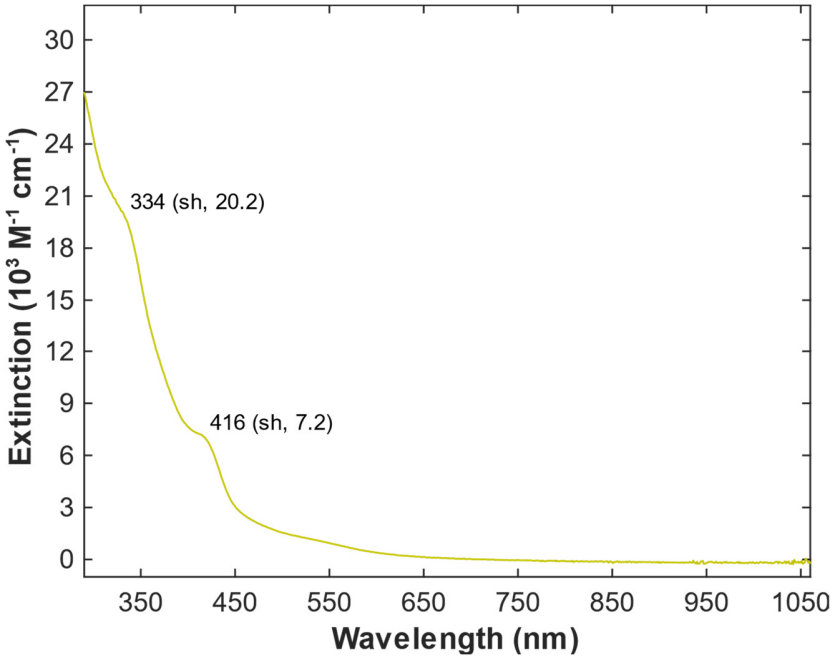


**Figure S9.**
UV-Vis electronic absorption spectrum of $2.3 \cdot 10^{-4}$ M toluene solution of **2**.

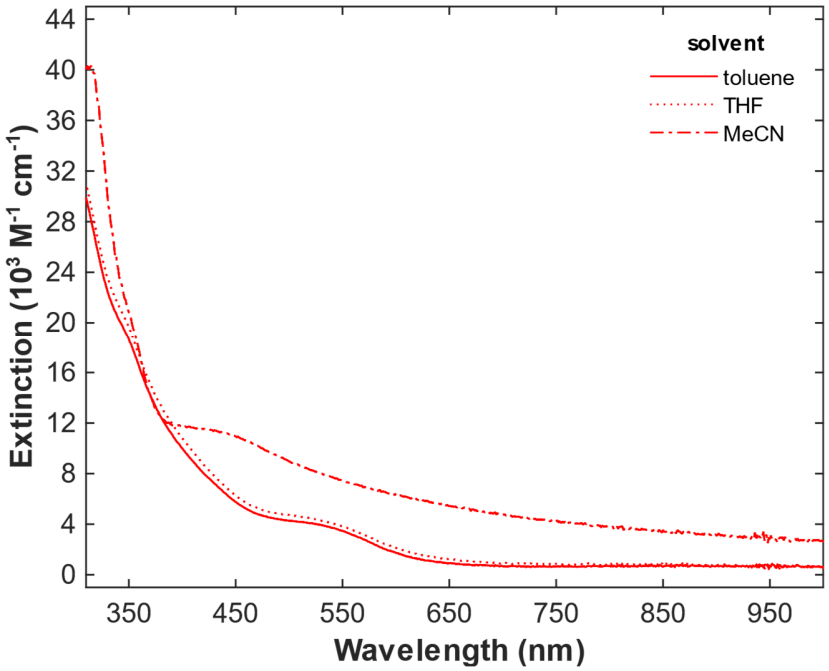


**Figure S10.**
UV-Vis electronic absorption spectrum of $1.1 \cdot 10^{-4}$ M solution of **3** in toluene (*solid red curve*), THF (*dotted red curve*) and acetonitrile (*dashed-dotted red curve*)

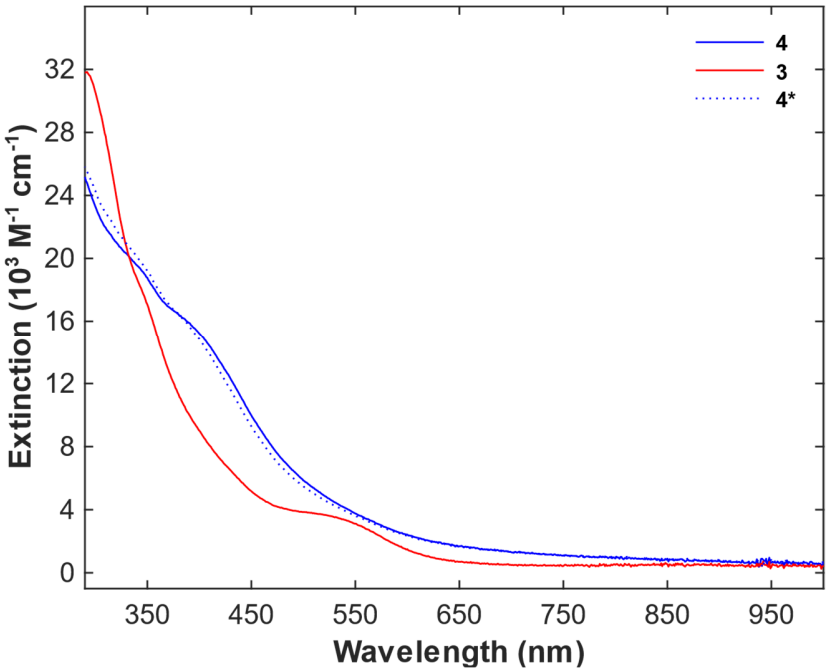


**FigureS11.**
Monitoring of the chemical reversibility of the $[Fe_4S_4]^{0/1+}$ (**3**/**4**) redox couple using UV-Vis absorption spectroscopy. The restoration of the expected UV-Vis signature of **4** (**4***) after re-oxidizing **3**, confirms chemical reversibility.

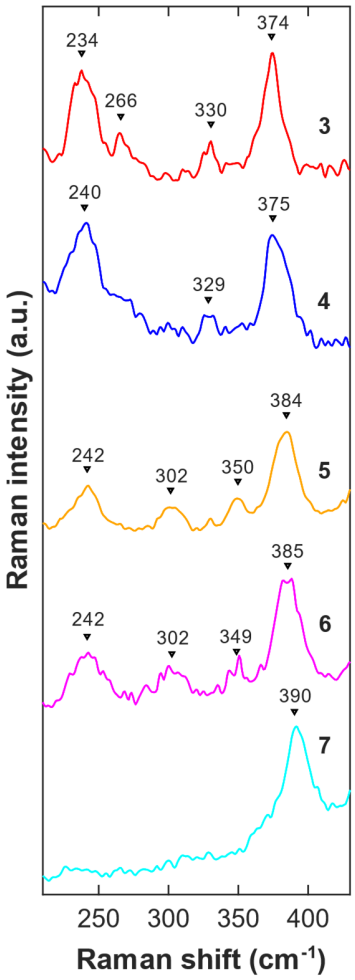


**Figure S12.**
Low-energy region of resonance Raman spectra recorded on powder samples of compounds **3** (*red*), **4** (*blue*), **5** (*yellow*), **6** (*magenta*) and **7** (*cyan*) recorded at room temperature with 532 nm laser excitation.

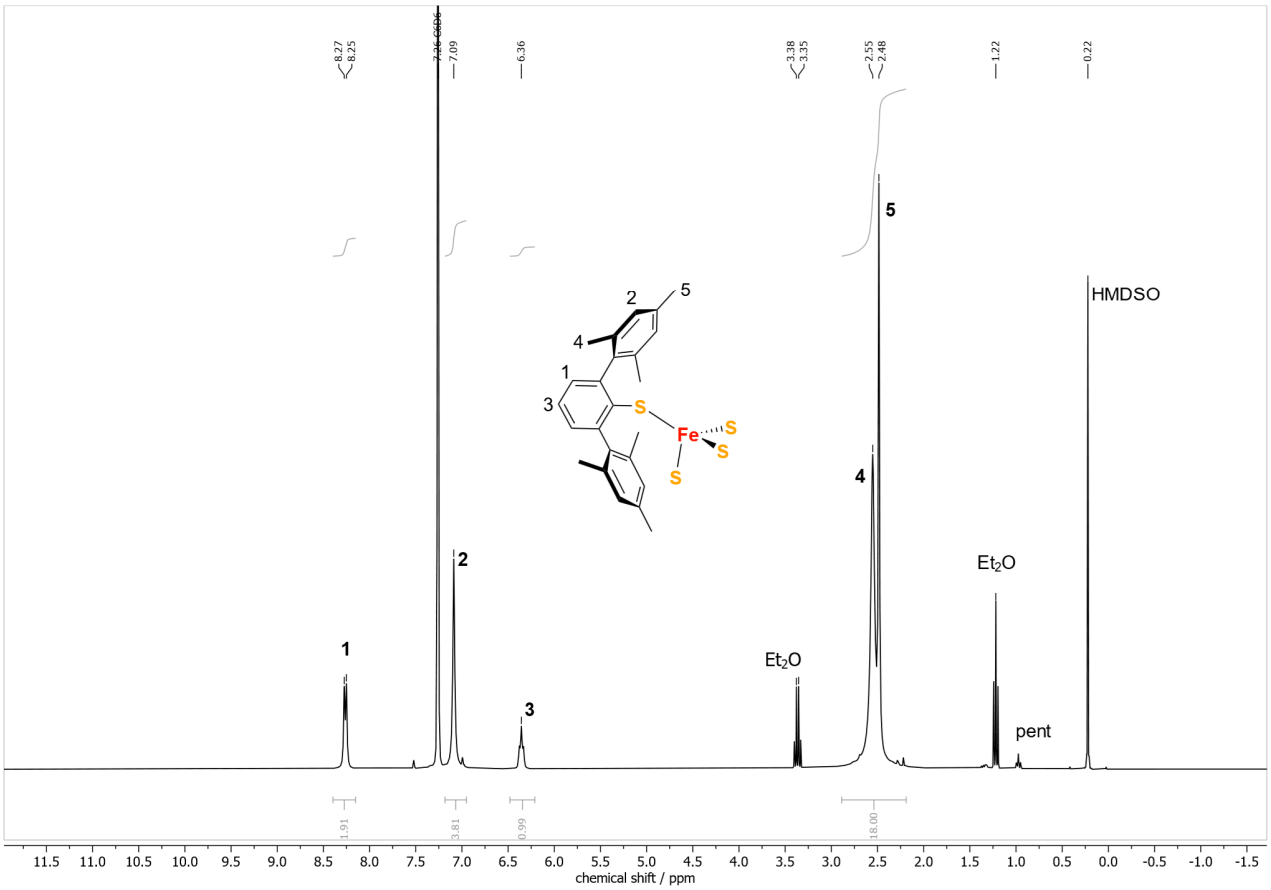


**Figure S13.**
$^{1}$H NMR spectrum of **5** recorded at 300 MHz at room temperature in $C_6D_6$.

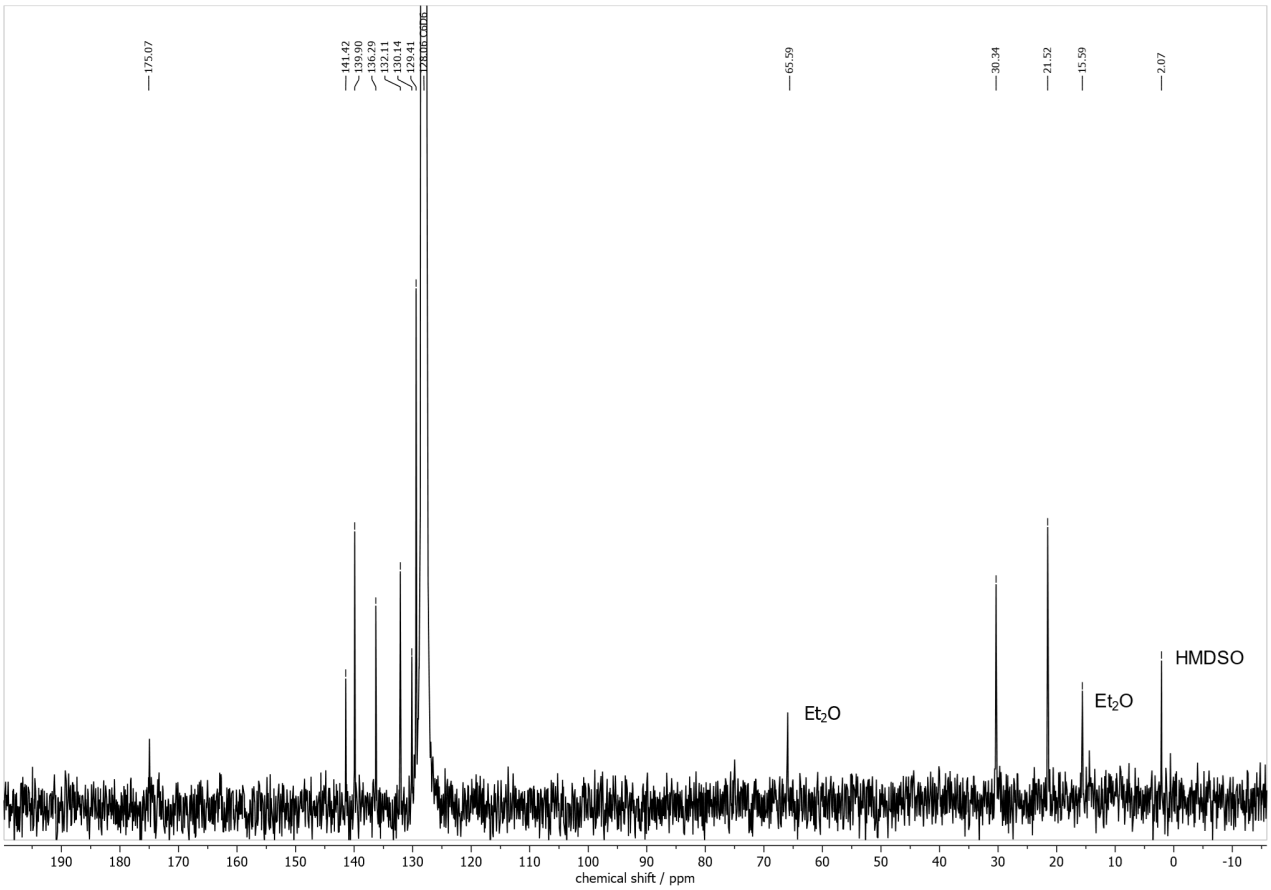


**Figure S14.**
$^{13}C$ NMR spectrum of **5** recorded at 75 MHz at room temperature in $C_6D_6$.

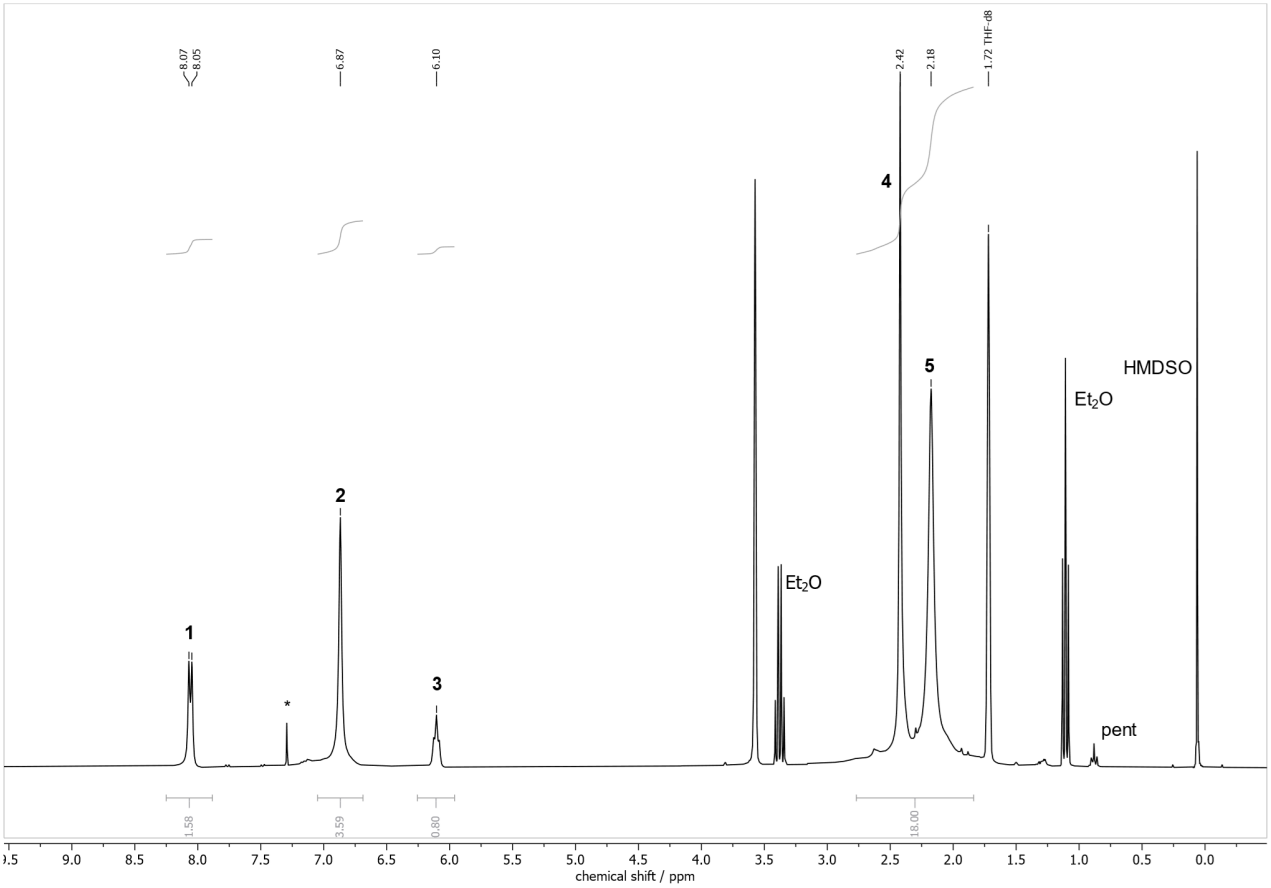


**Figure S15.**
$^{1}$H NMR spectrum of **5** recorded at 300 MHz at room temperature in THF-d8. Impurity peaks are marked by an asterisk.

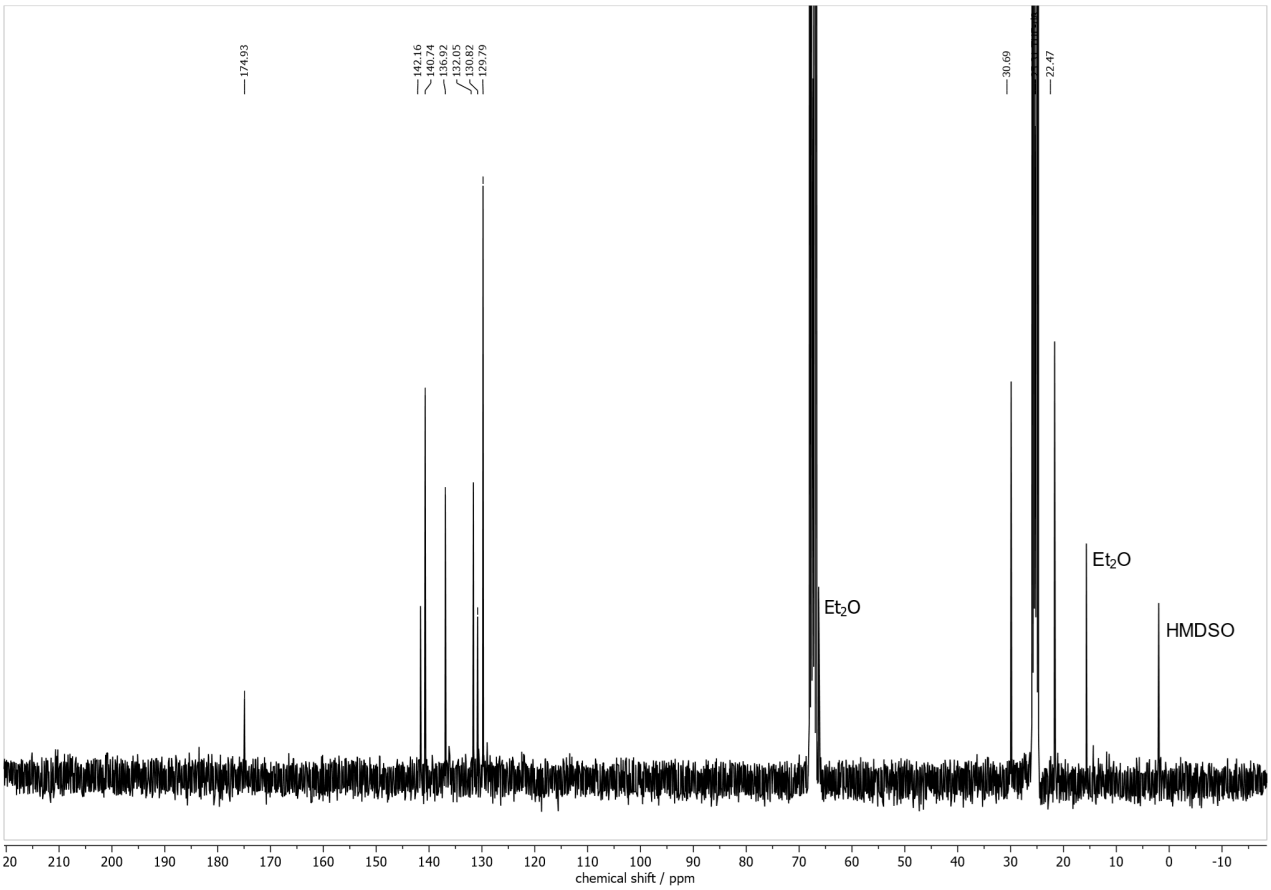


**Figure S16.**
$^{13}C$ NMR spectrum of **5** recorded at 75 MHz at room temperature in THF-d8.

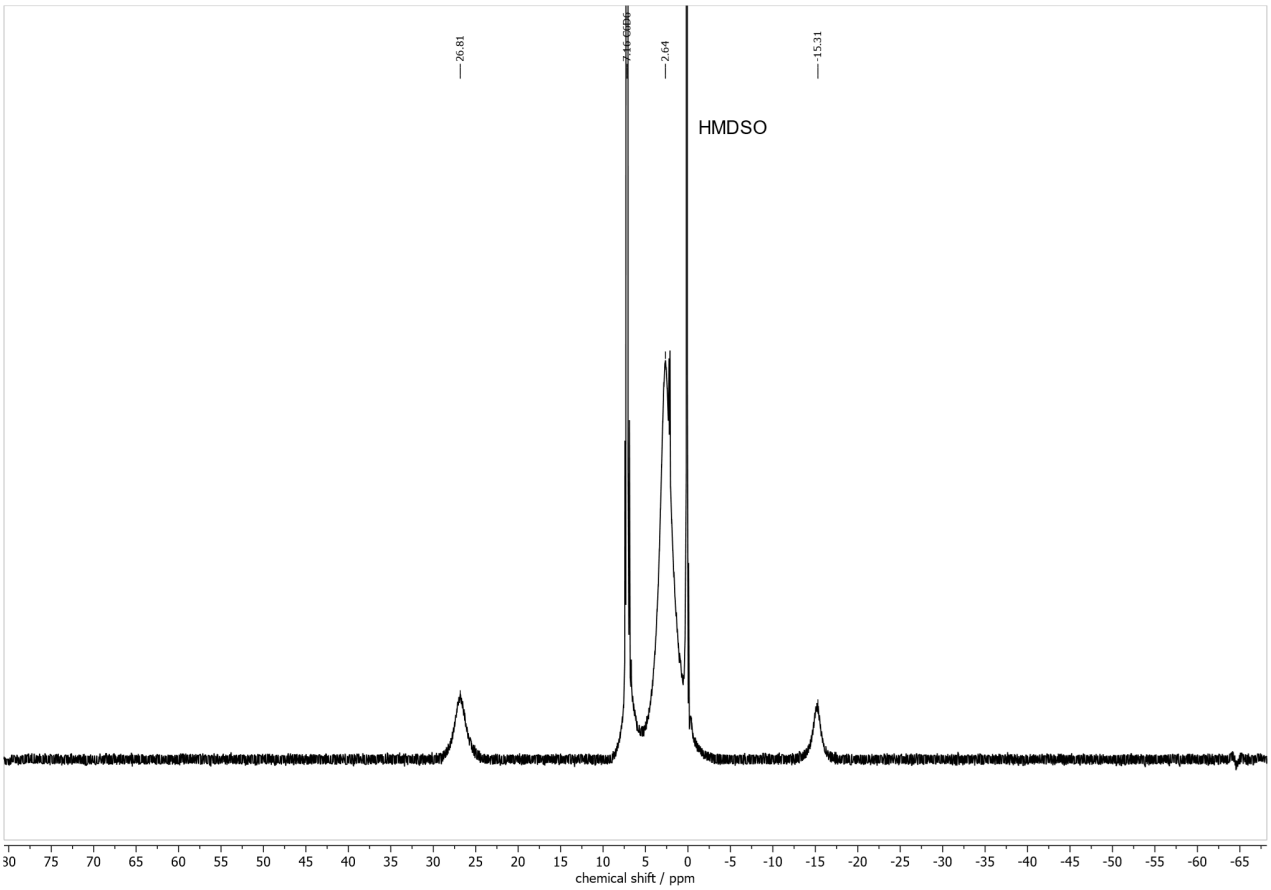


**Figure S17.**
$^{1}$H NMR spectrum of **3** recorded at 300 MHz at room temperature in $C_6D_6$.

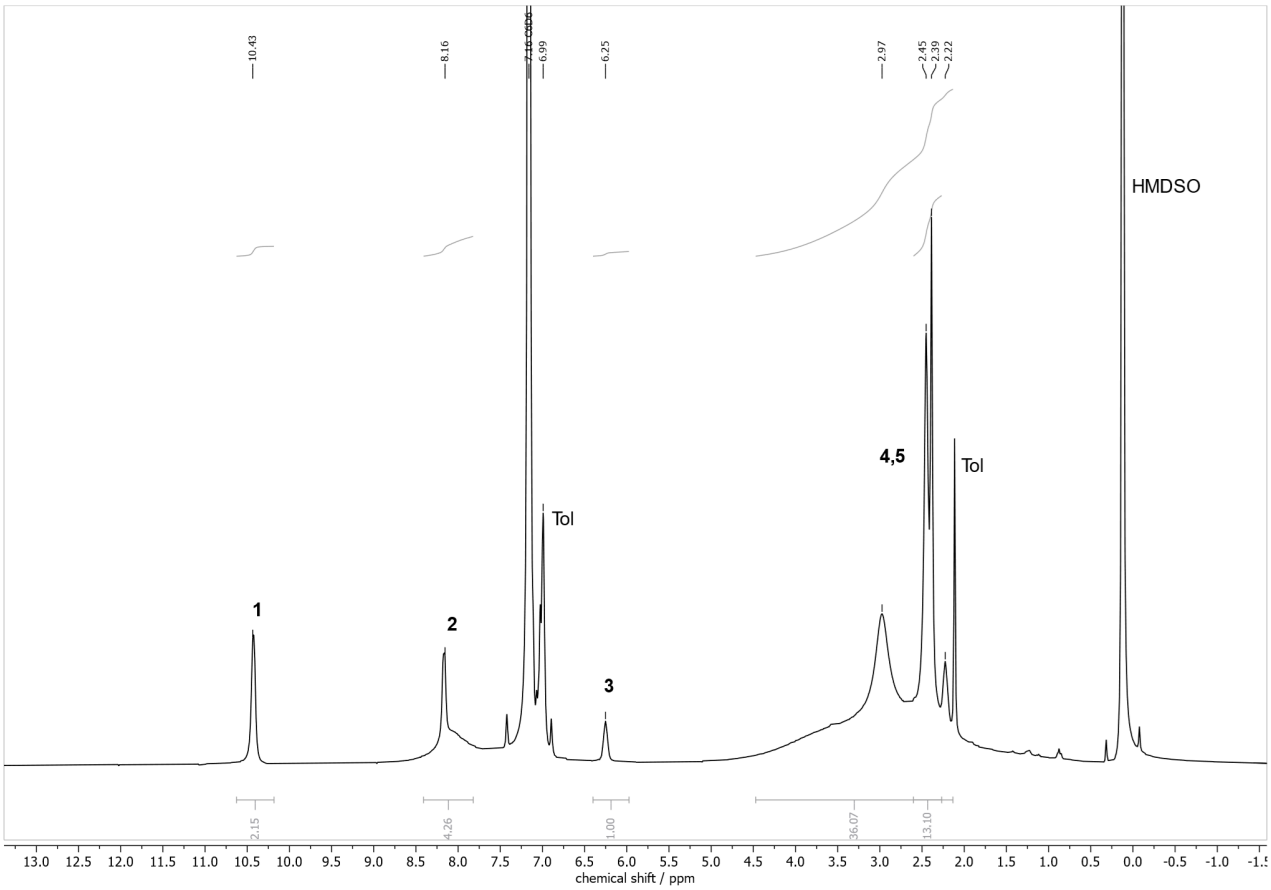


**Figure S18.**
$^{1}$H NMR spectrum of **4** recorded at 300 MHz at room temperature in $C_6D_6$.

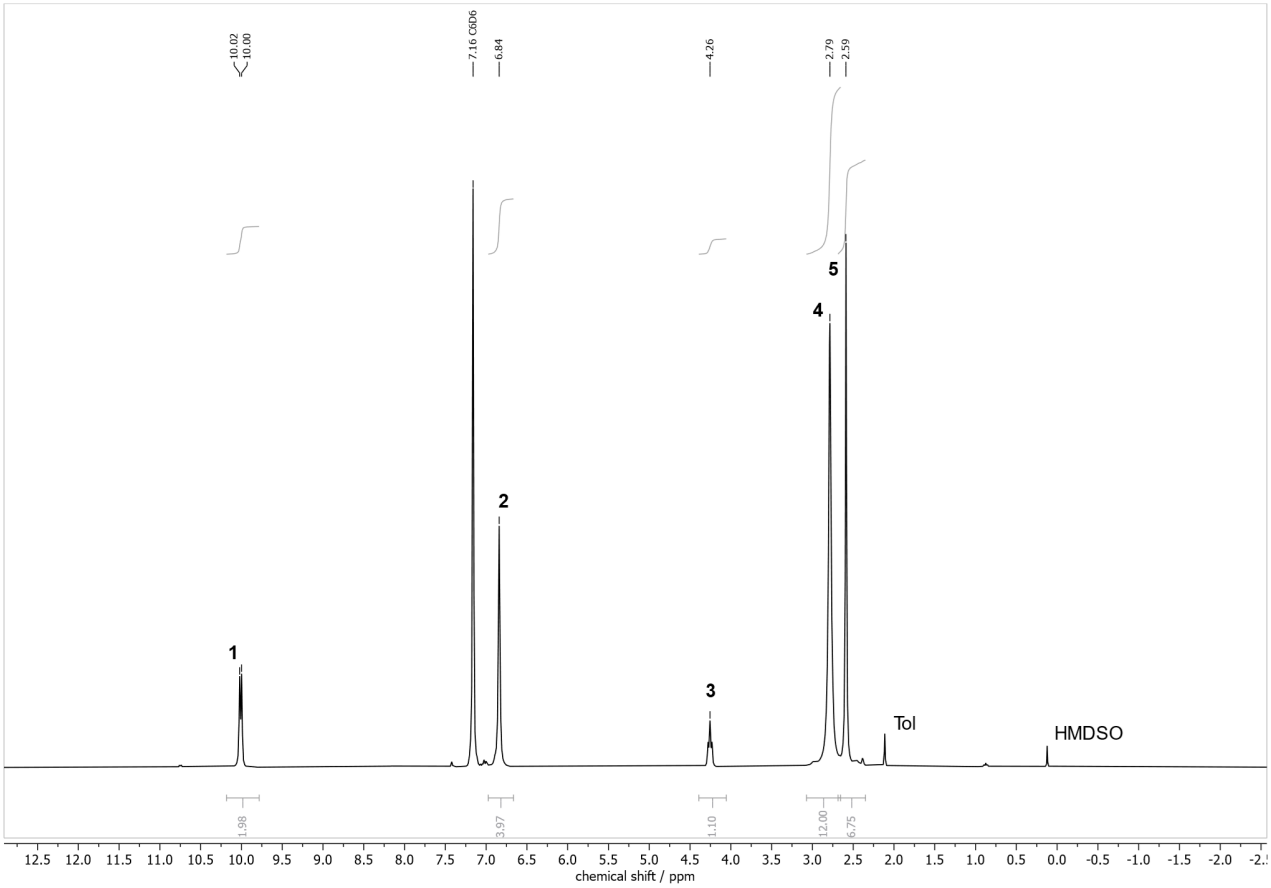


**Figure S19.**
$^{1}$H NMR spectrum of **6** recorded at 300 MHz at room temperature in $C_6D_6$.

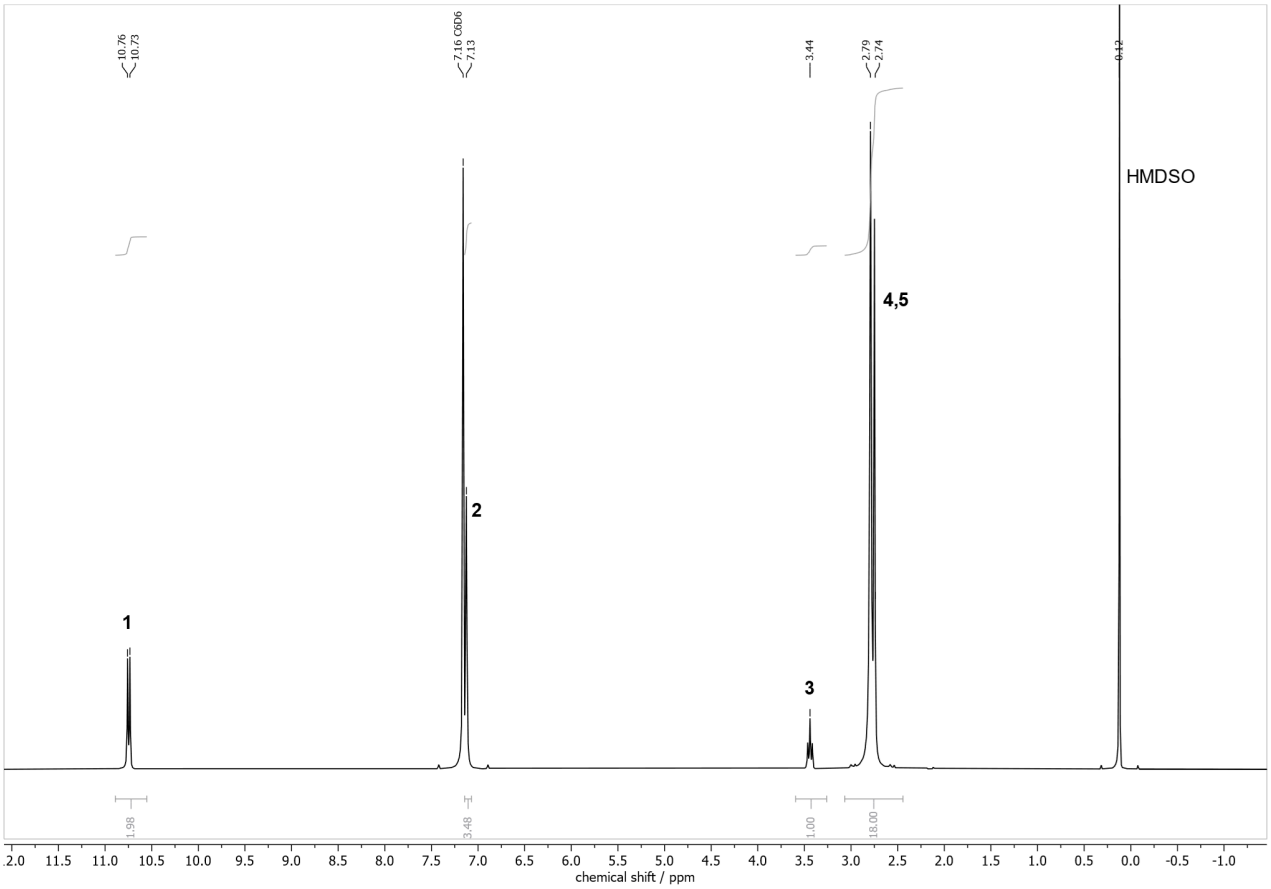


**Figure S20.**
$^{1}$H NMR spectrum of **7** recorded at 300 MHz at room temperature in $C_6D_6$.

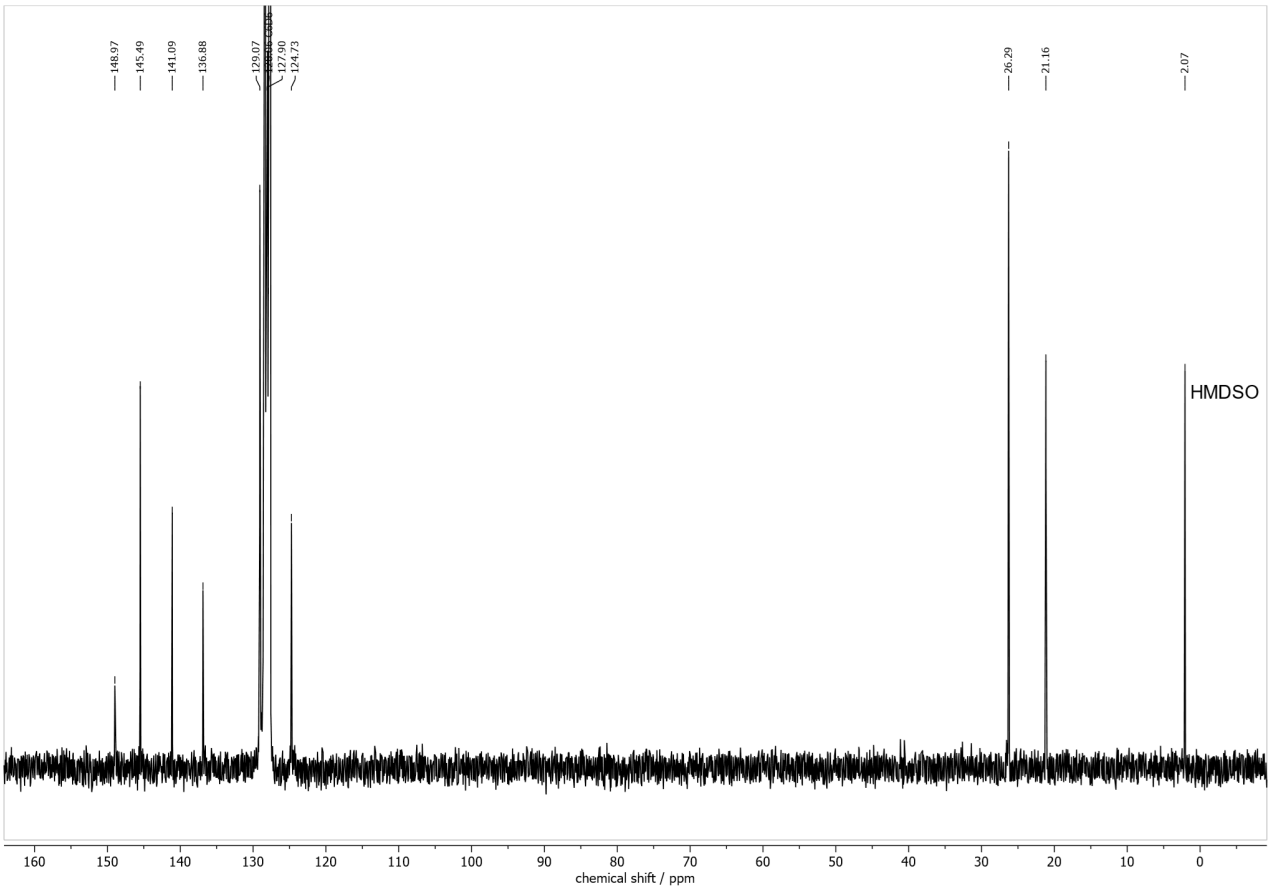


**Figure S21.**
$^{13}C$ NMR spectrum of **7** recorded at 75 MHz at room temperature in $C_6D_6$.

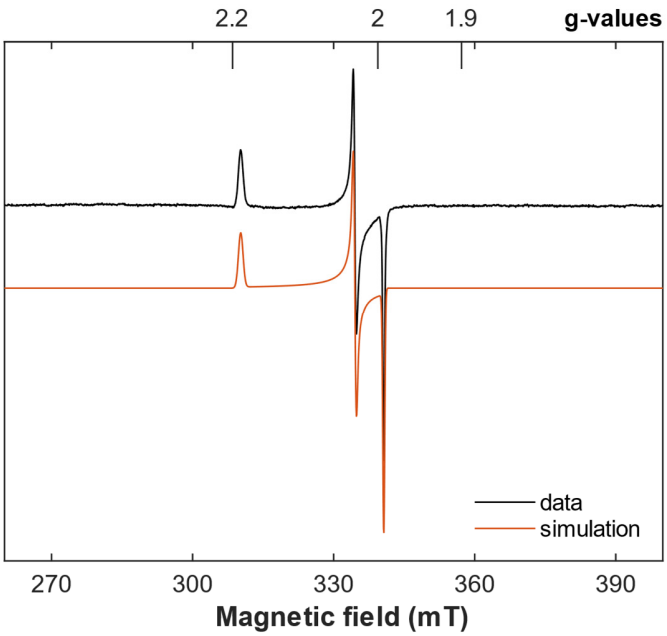


**Figure S22.**
X-band continuous wave EPR spectrum of a 2 mM frozen toluene solution of **1** recorded at 20 K ($\nu$=9.5 GHz; 54 dB microwave attenuation). The simulation for $S$=1/2 is shown in *red* color, revealing $g$-values of (2.188, 2.029, 1.993). Experimental data are black; an anisotropic $g$-distribution was used as broadening model.

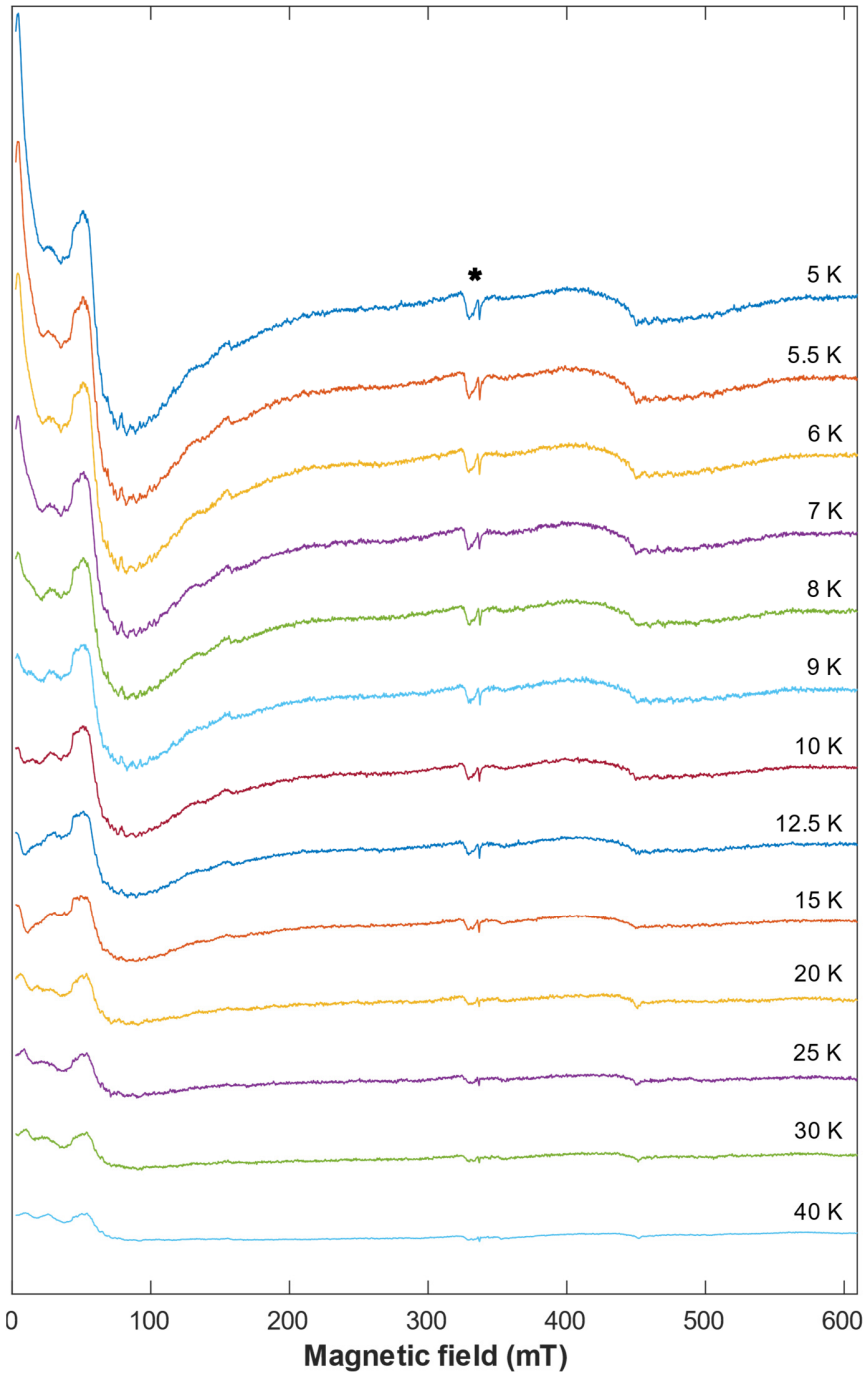


**Figure S23.**
X-band perpendicular-mode continuous wave EPR spectrum of a 2 mM toluene solution of **3** recorded at varying temperature (5 K to 40 K). The asterisk marks a spectral artefact of the resonator. The absence of a resonance signal around *g*=2 at temperatures down to 5 K supports the integer-spin nature and all-ferrous composition of **3**.

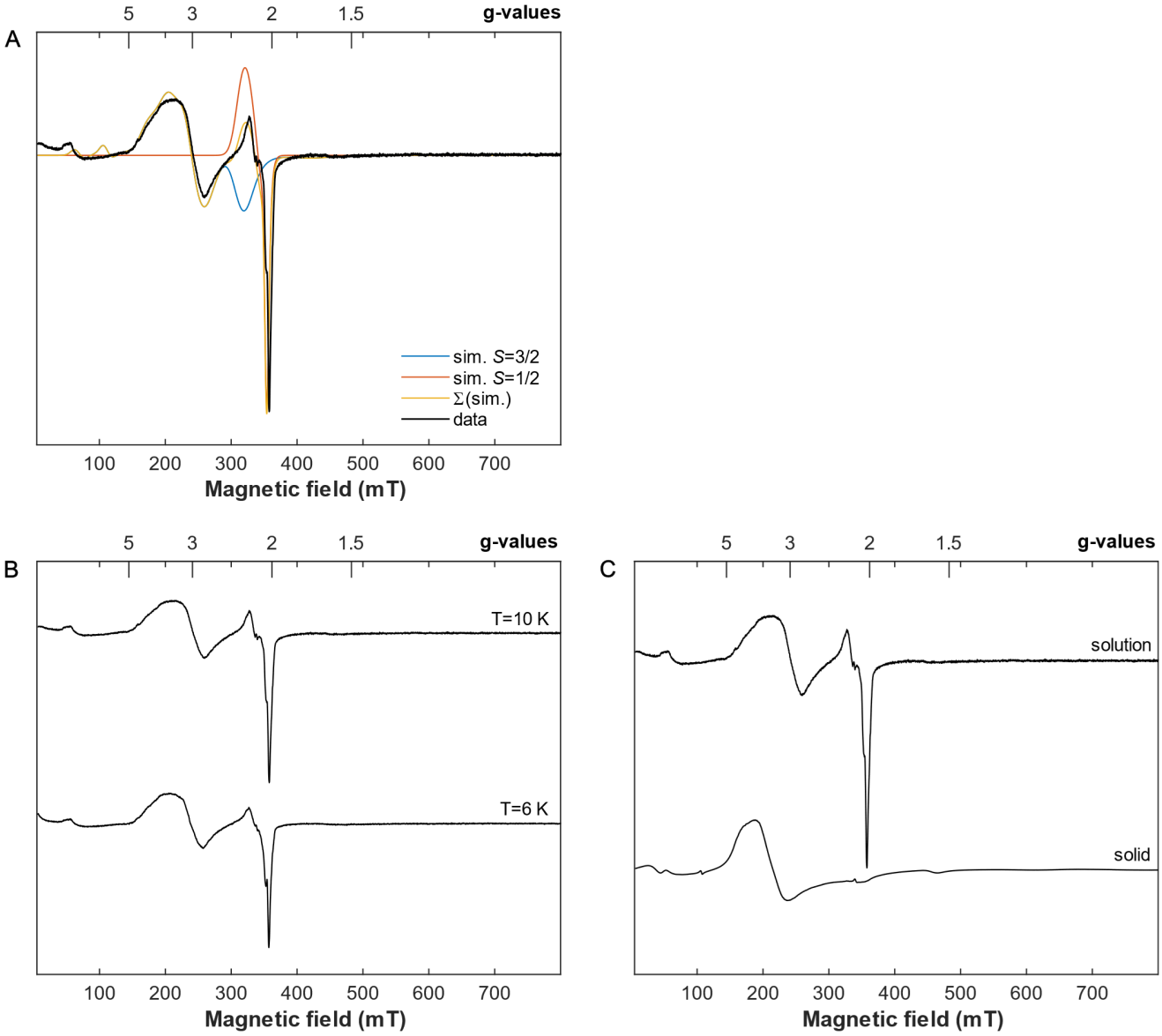


**Figure S24.**
EPR spectroscopic data for cluster **4**. (*A*) X-band continuous wave EPR spectrum of a 2 mM frozen toluene solution of **4** recorded at 10 K ($\nu$=9.5 GHz; 30 dB microwave attenuation). Experimental data are represented by a black trace, simulations are *red* (*S*=1/2), *blue* (*S*=3/2) and *yellow* (sum) respectively. The simulation parameters are: (*red*, *S*=1/2) *g*=(1.91, 1.98, 2.12) with 56 % weight and (*blue*, *S*=3/2) *g*=(3.05, 2.64, 2.16), *D*=(1812, 408) MHz with 44 % weight. (*B*) X-band continuous wave EPR spectra of **4** recorded at temperatures of 10 K (*n*=9.5 GHz; 30 dB microwave attenuation, *top*) and 6 K ($\nu$=9.5 GHz; 36 dB microwave attenuation, *bottom*), respectively. (*C*) Normalized X-band continuous wave EPR spectra of **4** recorded at 10 K on a 2 mM frozen toluene solution ($\nu$=9.5 GHz; 30 dB microwave attenuation, *top*) and on a powder immobilized in eicosane ($\nu$=9.5 GHz; 30 dB microwave attenuation, *bottom*).

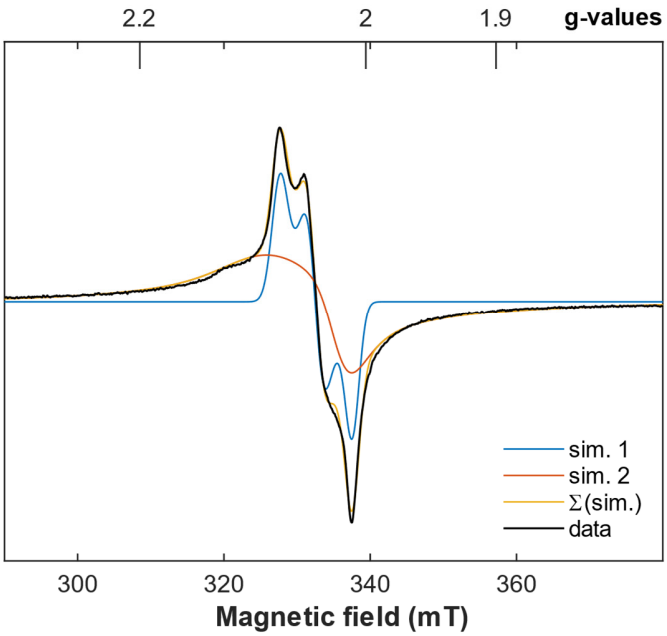


**Figure S25.**
X-band continuous wave EPR spectrum of a 2 mM frozen toluene solution of **6** recorded at 40 K ($\nu$=9.5 GHz; 30 dB microwave attenuation). Experimental data are represented by a black trace, simulations are *blue* (*S*=1/2), *red* (*S*=1/2) and *yellow* (sum) respectively. The simulation parameters are: (*red*, *S*=1/2) *g*=(2.07, 2.02, 2.00) with 87 % weight and an anisotropic gaussian *g*-distribution with full-width-at-half-maximum values (strains) of (0.077 0.022 0.466) and (*blue*, *S*=1/2) *g*=(2.07, 2.04, 2.01) with 13 % weight and *g*-strains of (0.016 0.016 0.013).

**Table S2.**
Nuclear parameters (in mm·s$^{-1}$) and contributions determined from the simulations of the 80 K / 60 mT Mössbauer spectra (Fig. 4*A*). Uncertainties are ±0.03 and ±0.05 mm·s$^{-1}$ for $\delta$ and $\Delta E_Q$, respectively. Note that the strong paramagnetism of **3** (*S*=4 ground state) leads to broad lines on the 80 K Mössbauer spectrum recorded with 60 mT. Accordingly, the zero-field 80 K spectrum was preferred for the comparison within the series.

| | parameter | site 1 | site 2 | site 3 | site 4 | av. |
|---|---|---|---|---|---|---|
| **3** / $[Fe_4S_4]^0$ | % | 25 | 25 | 25 | 25 | 0.62 |
| | $\delta$ | 0.61 | 0.71 | 0.57 | 0.59 | |
| | $\Delta E_Q$ | 2.88 | 2.10 | 1.51 | 0.82 | |
| | $\Gamma$[a,b] | 0.61 | 0.96 | 0.96 | 0.96 | |
| **4** / $[Fe_4S_4]^{1+}$ | % | 50 | 50 | | | 0.52 |
| | $\delta$ | 0.55 | 0.50 | | | |
| | $\Delta E_Q$ | 0.89 | 1.24 | | | |
| | $\Gamma$[a] | 0.32 | 0.41 | | | |
| **5** / $[Fe_4S_4]^{2+}$ | % | 50 | 50 | | | 0.46 |
| | $\delta$ | 0.44 | 0.49 | | | |
| | $\Delta E_Q$ | 0.74 | 0.87 | | | |
| | $\Gamma$[a] | 0.40 | 0.40 | | | |
| **6** / $[Fe_4S_4]^{3+}$ | % | 50 | 50 | | | 0.38 |
| | $\delta$ | 0.40 | 0.36 | | | |
| | $\Delta E_Q$ | 1.24 | 0.78 | | | |
| | $\Gamma$[a] | 0.36 | 0.32 | | | |
| **7** / $[Fe_4S_4]^{4+}$ | % | 100 | | | | 0.32 |
| | $\delta$ | 0.32 | | | | |
| | $\Delta E_Q$ | 1.02 | | | | |
| | $\Gamma$[a] | 0.34 | | | | |

[a] $\Gamma$ stands for the full-width at half-maximum.

[b] No satisfying simulation could be obtained with a common linewidth. A significant improvement was obtained assuming that one site presents a linewidth different from that of the other three.

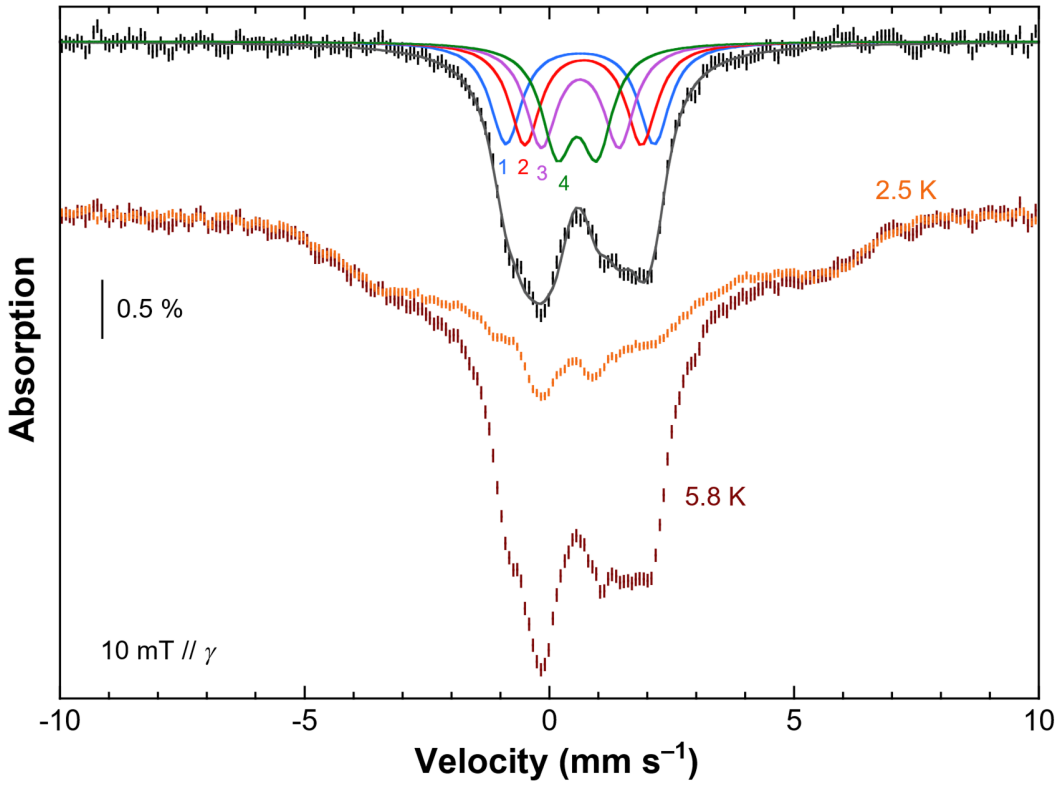


**Figure S26.**
Mössbauer spectra recorded on a powder sample of **3** at 5.8 K (*brown* hatched bars) and 2.5 K (*orange* hatched bars) using a 0.01 T external magnetic field applied parallel to the $\gamma$-beam. The 2.5 K spectrum is scaled for the subtraction. The difference spectrum displayed on the top (*black* hatched bars) was fairly reproduced assuming four doublets with parameters listed in Table S3.

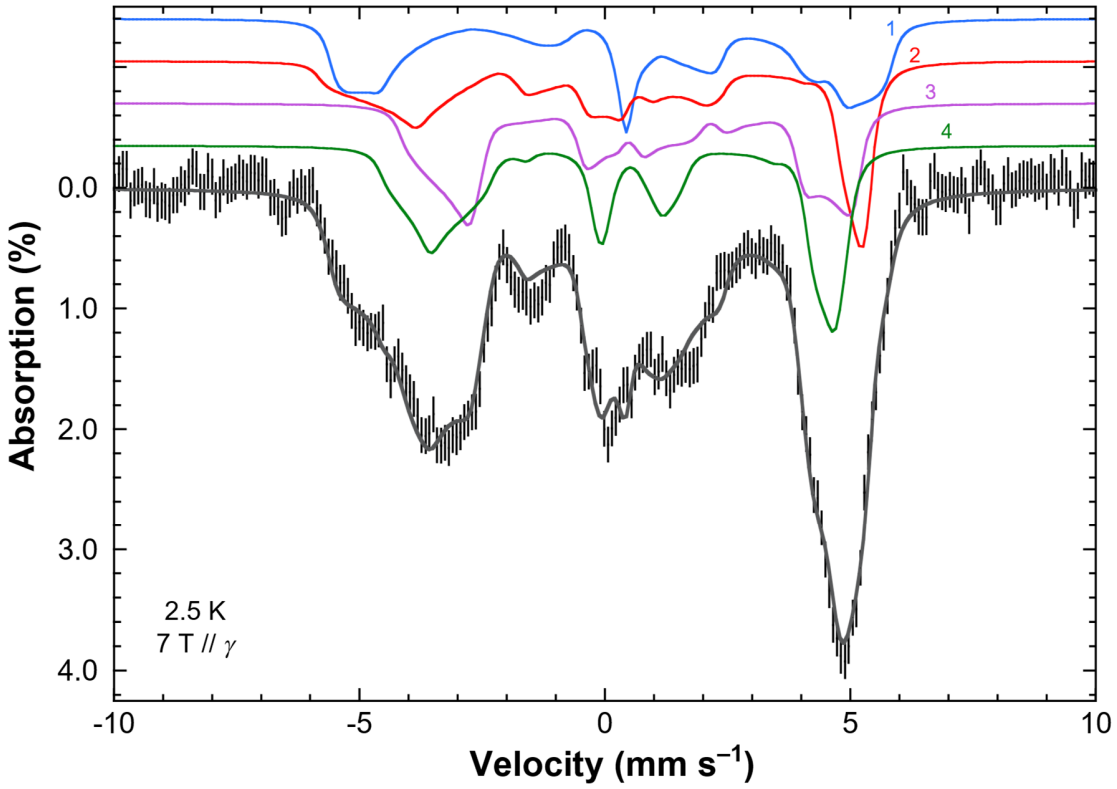


**Figure S27.**
2.5 K Mössbauer spectrum recorded on a powder sample of **3** using a 7 T external magnetic field applied parallel to the $\gamma$-beam (*hatched bars*). A simulation is overlaid as a grey solid line. The contributions of Sites 1-4 are displayed above as *blue*, *red*, *mauve* and *green* thin lines respectively.

**Table S3.**
Electronic and nuclear parameters for the simulations of the Mössbauer spectra of compound **3**. A $S$=4 state was assumed. All tensors are expressed in the ZFS principal axis frame. Because this tensor is common to the four sites, the rhombicity parameter, $\eta$, of the EFG may present values outside the usual domain (0-to-1). It should be underlined that the magnetic theoretical spectra are dependent on a high number of parameters. Different sets should lead to equally satisfying simulations. To evidence the $S$=4 state, simulations were performed assuming colinear tensors and one of those is presented here.

| parameter | site 1 | site 2 | site 3 | site 4 |
|---|---|---|---|---|
| $\delta$ / mm·s$^{-1}$ | 0.63 | 0.69 | 0.63 | 0.57 |
| $\Delta E_Q$ / mm·s$^{-1}$ | –3.03 | 2.39 | 1.59 | 0.81 |
| $\eta$ | 0.98 | 1.02 | 1.35 | 1.02 |
| $D$ / cm$^{-1}$ | | –0.22 | | |
| $E/D$ | | 0.33 | | |
| $g_{x,y,z}$ | | 2.0/2.0/2.0 | | |
| $A_{x,y,z}$ / ($g_n\mu_n$) / T | 5.6/1.1/5.7 | –8.2/–10.2/–6.3 | –6.3/–8.0/–7.8 | –8.1/–9.2/–6.7 |
| $\Gamma$ / mm·s$^{-1}$ | 0.33 | 0.33 | 0.33 | 0.33 |
| contribution | 25 % | 25 % | 25 % | 25 % |

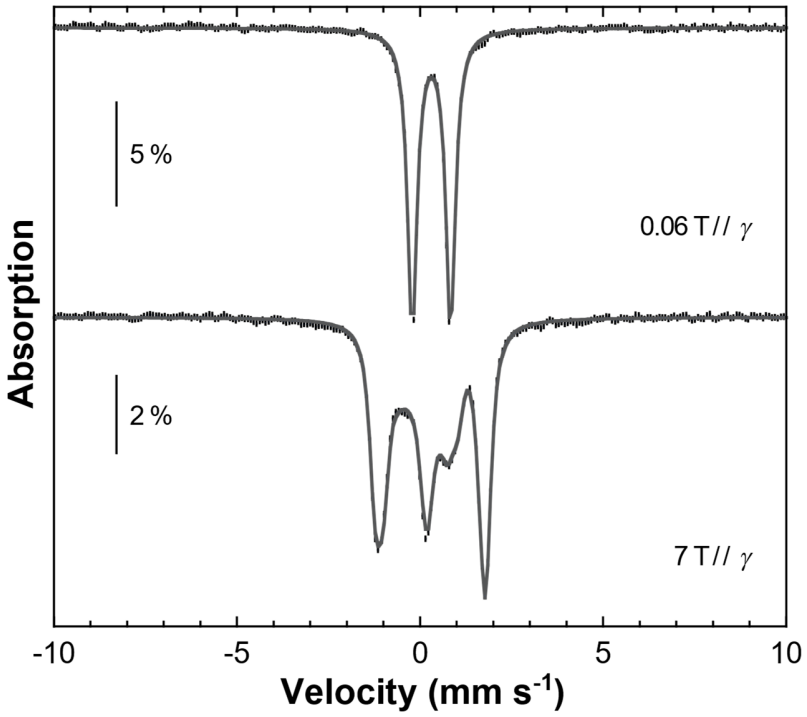


**Figure S28.**
5.3 K Mössbauer spectrum recorded on a powder sample of **7** using a 0.06 T (*top*) and 7 T (*bottom*) external magnetic field applied parallel to the $\gamma$-beam (hatched bars). Simulations are overlaid as a *grey* solid lines assuming a $S$=0 state with the following parameters: $\delta$=0.31 mm s$^{-1}$, $\Delta E_Q$=–1.05 mm s$^{-1}$, $\eta$=0.48, $\Gamma_{fwhm}$=0.31 mm s$^{-1}$. An impurity accounting for 4 % of the total Fe content has been subtracted ($\delta$=0.96 mm s$^{-1}$, $\Delta E_Q$=2.09 mm s$^{-1}$, $\eta$=0, $\Gamma_{fwhm}$=0.26 mm s$^{-1}$).

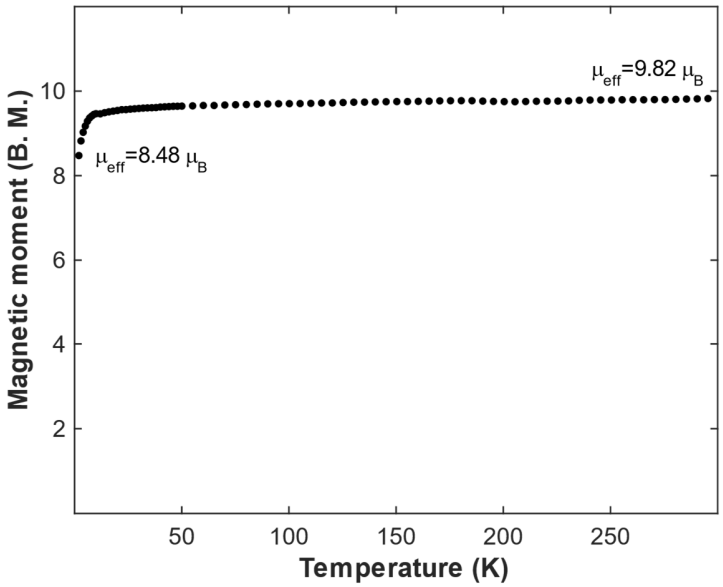


**Figure S29.**
Variable-temperature SQUID magnetization data recorded on a powdered sample of **3**. Experimental data are represented as black dots, and exhibit effective magnetic moments, $\mu_{eff}$, of 8.48 $\mu_B$ at 2 K and 9.82 $\mu_B$ at 300 K, respectively. The measurement was performed at fixed magnetic field (5 mT) and varying temperature *T* (from 2 to 300 K).

**Crystallographic Details**

Black, block-shaped crystals of $K_2[Fe_2S_2(DmpS)_4]\cdot Et_2O$ (**2**) were grown by slow evaporation of diethyl ether from a diethyl ether/HMDSO (1:1) mixture. Black, needle-shaped crystals of $K_4[Fe_4S_4(DmpS)_4]\cdot 2HMDSO$ (**3**) were grown by layering a toluene solution with an equivalent amount of HMDSO at room temperature. Black, hexagonal rod-shaped crystals of $K_2[Fe_4S_4(DmpS)_4]\cdot 2HMDSO$ (**5**) were grown by layering HMDSO with a diisopropyl ether solution at room temperature. Black, needle-shaped crystals of $K_3[Fe_4S_4(DmpS)_4]\cdot 2HMDSO$ (**4**) were grown by layering a toluene solution with HMDSO at room temperature. Dark brownish green block-shaped crystals of $K[Fe(DmpS)_2]\cdot C_7H_8$ (**1**) were grown by layering a toluene solution with cold pentane at -30°C. Black, prism-shaped crystals of $K[Fe_4S_4(DmpS)_4]\cdot C_7H_8$ (**6**) were grown by layering a saturated toluene solution with excess HMDSO at room temperature. Black, block-shaped crystals of $[Fe_4S_4(DmpS)_4]\cdot C_6H_{18}Si_2O$ (**7**) were grown from a dilute hot HMDSO solution upon standing at room temperature for 1 week in an undisturbed location.
The suitable crystals were embedded in perfluoropolyalkylether oil inside an argon-filled glovebox equipped with a microscope. Subsequently, they were transferred from a sealed vessel under argon into the cold nitrogen gas stream of the diffractometer as fast as possible. Intensity data of all investigated compounds were collected at 100 K using Mo-$K_\alpha$ radiation.

Data for $K_2[Fe_2S_2(DmpS)_4]\cdot Et_2O$ (**2**), $K_2[Fe_4S_4(DmpS)_4]\cdot 2HMDSO$ (**5**), $K_3[Fe_4S_4(DmpS)_4]\cdot 2HMDSO$ (**4**) and $K_4[Fe_4S_4(DmpS)_4]\cdot 2HMDSO$ (**3**) were collected on a Bruker Venture D8 diffractometer equipped with a Bruker Photon II detector. Data for $K[Fe(DmpS)_2]\cdot C_7H_8$ (**1**) were collected on an Oxford XCalibur S diffractometer with Sapphire 3 CCD detector. Data for $K[Fe_4S_4(DmpS)_4]\cdot C_7H_8$ (**6**) were collected on a Bruker Smart Apex2 diffractometer with Apex2 CCD detector. Lastly, data for $[Fe_4S_4(DmpS)_4]\cdot C_6H_{18}Si_2O$ (**7**) on a Rigaku XtaLAB Synergy S diffractometer with Dualflex HyPix-6000HE detector. All measurements were performed using Mo-$K_\alpha$ radiation.

After data collection, structures were solved by intrinsic phasing (SHELXT) and refined by full-matrix least-squares procedures on $F^2$ using SHELXL in the *olex2* program suite (21-24). All non-hydrogen atoms were refined with anisotropic displacement parameters. The hydrogen atoms were placed in positions of optimized geometry.
Crystallographic data, data collection and structure refinement details for the crystal structure determinations are given in Table S10. Representations of the molecular structures are shown in Fig. S30-S36 & S41.

*Remarks:* The data for **5** could be solved either in tetragonal space-group $P\bar{4}2_1c$ (No. 114) with an occupancy of the K-site of 0.5 (which corresponds to 2 K atoms per molecule) or in the orthorhombic space group $P2_12_12$ (No. 18) with full occupancy of the K-site (also equivalent to 2 K-atoms per molecule). The final refinement was performed as a twin (matrix 0 1 0 1 0 0 0 0 $\bar{1}$). The volume ratio of the individuals refined to about 0.44:0.56 and the R1-value dropped from 10 % to 3.33 %.
Overall, the molecule **5** shows pseudosymmetry. Accordingly, refinement in the space group $P\bar{4}2_1c$ (No. 114) (as it was successfully performed for compounds **3** and **4**) leads to a high R1-value (about 16 %) with unreasonable displacement parameters. Therefore, the description as an orthorhombic twin was chosen.

In **4**, structural differences appeared to be less significant, and hence, a good fit could be obtained in the tetragonal space-group $P\bar{4}2_1c$ (No. 114) with an occupancy of the K-site of 0.75. A free refinement of the occupancy converges at 0.747(9).

The unit cell of **6** contains a molecule of toluene, which is disordered over two sites. The corresponding ellipsoids were split and refined in two parts with fractional occupancies of 0.5:0.5. Additionally, three reflections (hkl 0 0 1) were partially covered by the beamstop and omitted from the refinement.

For compound **2**, 12 reflections at low angles were omitted because they were partially covered by the beamstop. Likewise, for compound **7**, 18 reflections at low angles were omitted for the same reason.

The data of compound **3** can be solved and refined straightforwardly in tetragonal space-group $P\bar{4}2_1c$ (No. 114) affording satisfying structural parameters on a first glance, examples of which are summarized in Fig. S33 and Table S5. However, on a closer look, we found that this does not correspond to the physical reality, which is why this system was reinvestigated by collecting data sets at different temperatures (100 K–275 K). Therefore, the

details are described below in text (section titled “Crystallographic Identification of the Unique Iron Site in **3**” of this Supporting Material).

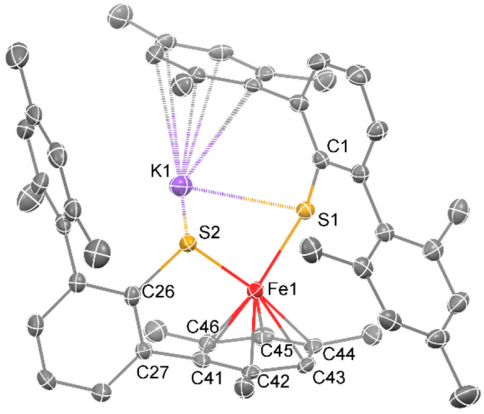


**Figure S30.**
Solid-state molecular structure of **1** in crystals of **1**·$C_7H_8$. Hydrogen atoms and one co-crystallized molecule of toluene have been omitted for clarity; ORTEP thermal ellipsoids are shown at the 50% probability level. Selected bond lengths and angles are Fe1–S2 2.2450(9) Å, Fe1–S1 2.270(1) Å, Fe1–$h^6_{mes}$ 1.547 Å, S1–Fe1–S2 95.37(3)°, C27–C46–C44 165.4(2)°.

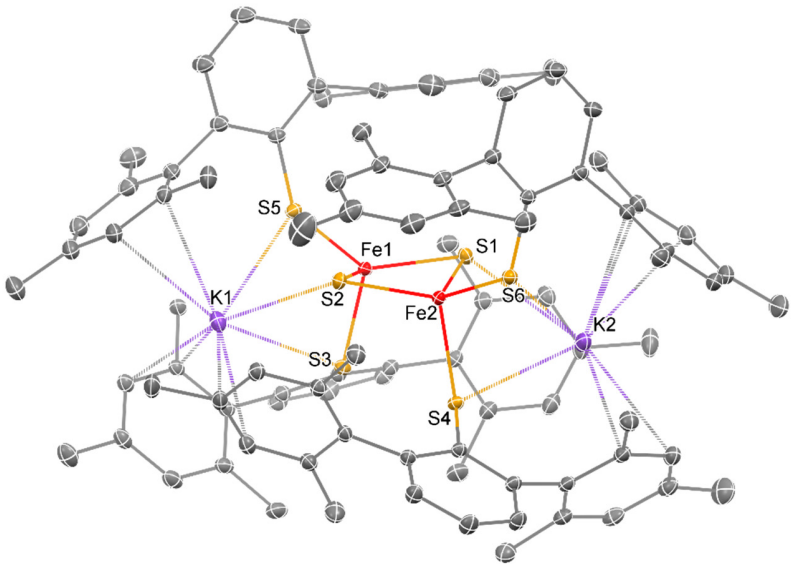


**Figure S31.**
Solid-state molecular structure of **2** in crystals of **2**·$C_4H_{10}O$. Hydrogen atoms and one co-crystallized molecule of diethyl ether have been omitted for clarity; ORTEP thermal ellipsoids are shown at the 50 % probability level. Selected bond lengths and angles are Fe1–Fe2 2.6710(6) Å, Fe1–S1 2.2008(8) Å, Fe1–S2 2.2106(4) Å, Fe1–S3 2.359(1) Å, Fe1–S5 2.3090(4) Å, Fe2–S1 2.2064(4) Å, Fe2–S2 2.2050(6) Å, Fe2–S4 2.347(1) Å, Fe2–S6 2.306(1) Å, Fe1–S1–Fe2 74.61(2)°, Fe1–S2–Fe2 74.44(2)°.

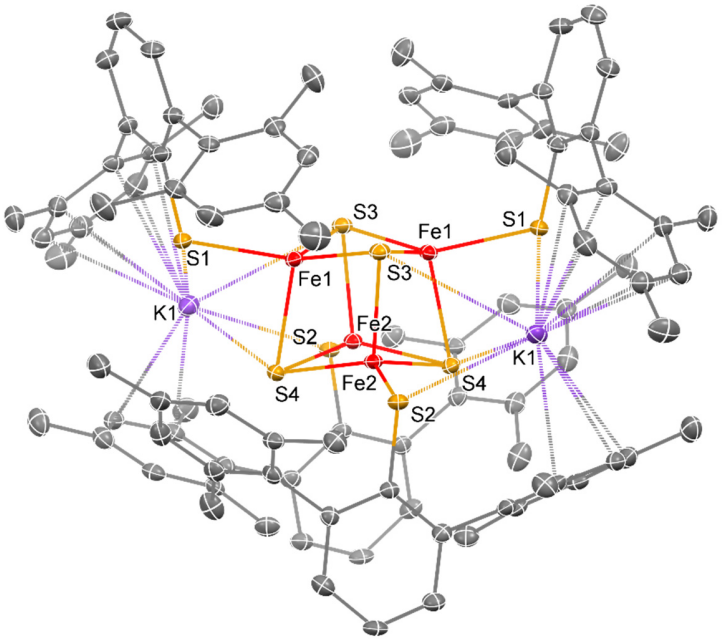


**Figure S32.**
Solid-state molecular structure of **5** in crystals of **5**·2$C_6H_{18}Si_2O$. Hydrogen atoms and two co-crystallized molecules of HMDSO have been omitted for clarity; ORTEP thermal ellipsoids are shown at the 50 % probability level. Selected bond lengths and angles are summarized in Table S4.

**Table S4.**
Summary of selected bond lengths and angles for the solid-state molecular structure of compound **5**.

| **property / Å or °** | **5** |
|---|---|
| Fe1–Fe1' | 2.7490(9) |
| Fe1–Fe2 | 2.7163(9) |
| Fe1'–Fe2 | 2.7729(9) |
| Fe2–Fe2' | 2.7303(9) |
| Fe1–S1 | 2.280(1) |
| Fe1–S3 | 2.243(1) |
| Fe1–S3' | 2.292(1) |
| Fe2–S2 | 2.271(1) |
| Fe2–S4 | 2.274(1) |
| Fe2–S4' | 2.261(1) |
| Fe1–S4 | 2.343(1) |
| Fe2–S3 | 2.331(1) |
| Fe–S–Fe | 74.63(4) |
| | 74.61(4) |
| | 71.97(4) |
| | 72.06(4) |
| | 74.02(4) |
| | 74.04(4) |
| S–Fe–S | 115.78(5) |
| | 132.84(5) |
| | 102.57(5) |
| | 119.62(5) |
| | 127.44(5) |
| | 102.95(5) |
| Fe–Fe–Fe | 59.65(2) |
| | 60.10(2) |
| | 60.97(2) |
| | 59.15(2) |
| | 61.21(2) |
| | 58.93(2) |

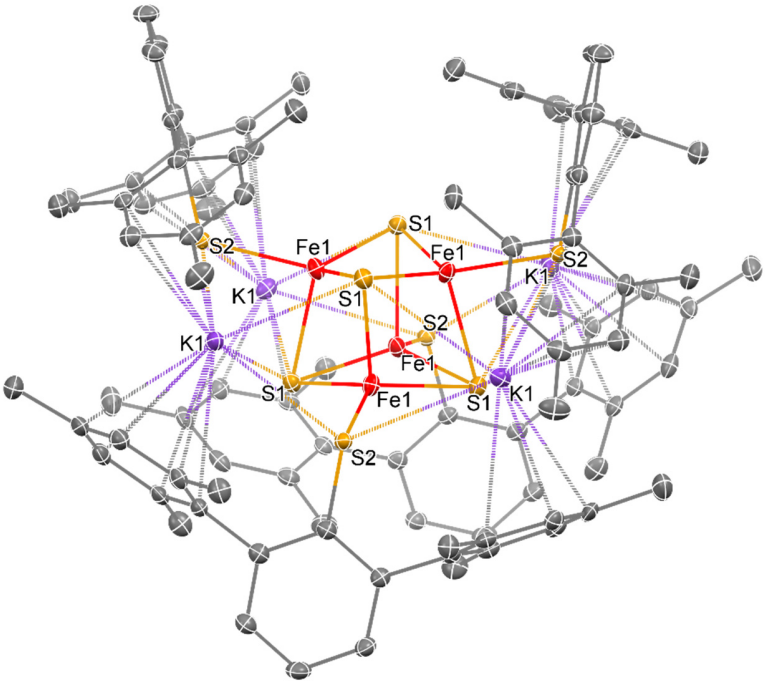


**Figure S33.**
Solid-state molecular structure of **3** in crystals of **3**·2$C_6H_{18}Si_2O$ without split-refinement of Fe1. Hydrogen atoms and two co-crystallized molecules of HMDSO have been omitted for clarity; ORTEP thermal ellipsoids are shown at the 50 % probability level. Selected bond lengths and angles are summarized in Table S5.

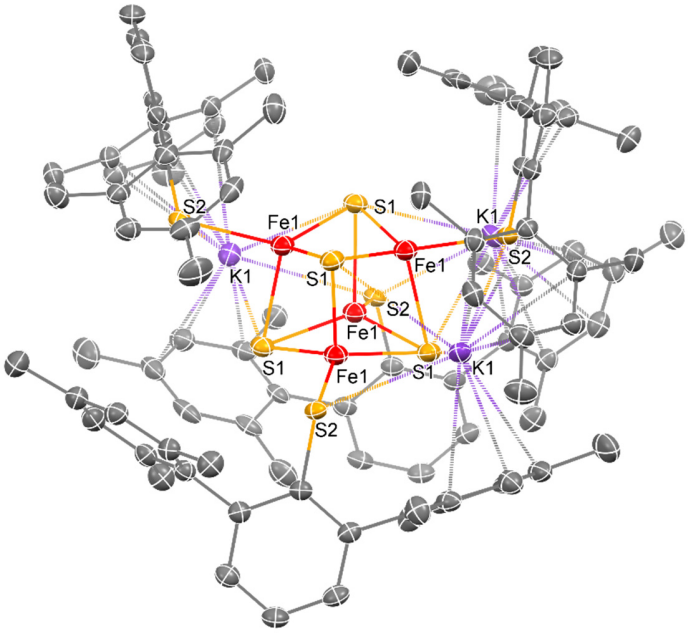


**Figure S34.**
Solid-state molecular structure of **4** in crystals of **4**·2$C_6H_{18}Si_2O$. Hydrogen atoms, two co-crystallized molecules of HMDSO and an arbitrary K-site have been omitted for clarity; ORTEP thermal ellipsoids are shown at the 50 % probability level. Selected bond lengths and angles are summarized in Table S5.

**Table S5.**
Summary of selected bond lengths and angles for the solid-state molecular structures of compounds **3** and **4**.

| property / Å or ° | 3 | 4 |
|---|---|---|
| Fe1–S1 | 2.319(1) | 2.294(1) |
| Fe1–S1' | 2.286(1) | 2.266(1) |
| Fe1–S1'' | 2.3997(9) | 2.3751(9) |
| Fe1–S2 | 2.3443(8) | 2.3033(9) |
| Fe1–Fe1' | 2.6187(6) | 2.6799(6) |
| Fe1–Fe1'' | 2.6920(7) | 2.7307(7) |
| Fe–S–Fe | 69.32(3) | 71.56(3) |
| | 69.55(3) | 71.98(3) |
| | 70.09(3) | 72.04(3) |
| S–Fe–S | 118.29(3) | 120.36(4) |
| | 107.32(3) | 105.01(4) |
| | 124.75(3) | 125.57(4) |
| Fe–Fe–Fe | 60.90(2) | 60.61(2) |
| | 58.21(2) | 58.77(2) |

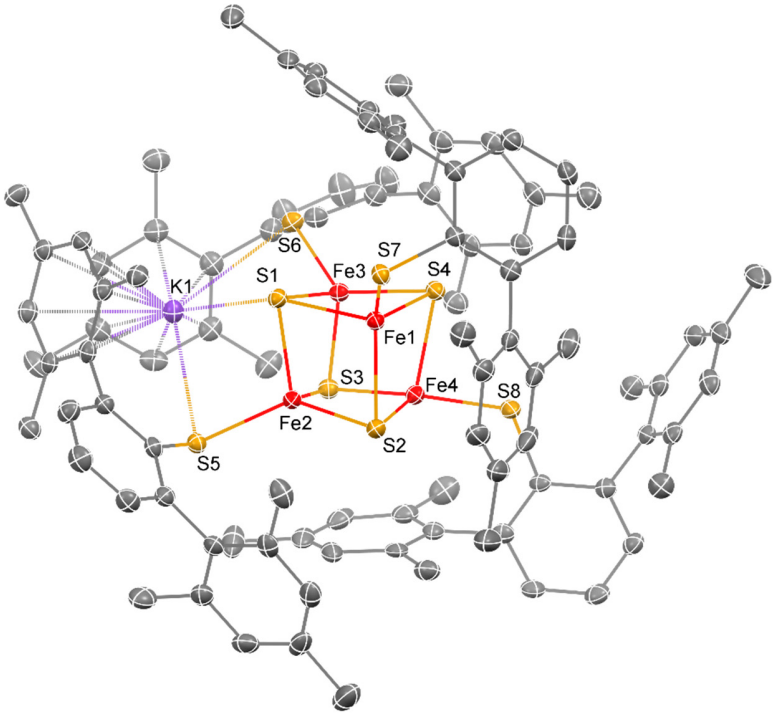


**Figure S35.**
Solid-state molecular structure of **6** in crystals of **6**·$C_7H_8$. Hydrogen atoms and one disordered co-crystallized molecule of toluene have been omitted for clarity; ORTEP thermal ellipsoids are shown at the 50 % probability level. Selected bond lengths and angles are summarized in Table S6.

**Table S6.**
Summary of selected bond lengths and angles for the solid-state molecular structure of compound **6**.

| property / Å or ° | 6 |
|---|---|
| Fe1–Fe2 | 2.8350(7) |
| Fe1–Fe3 | 2.7582(6) |
| Fe1–Fe4 | 2.8144(6) |
| Fe2–Fe3 | 2.7616(7) |
| Fe2–Fe4 | 2.7356(5) |
| Fe3–Fe4 | 2.7609(6) |
| Fe1–S1 | 2.2748(8) |
| Fe1–S2 | 2.3198(9) |
| Fe1–S4 | 2.1964(7) |
| Fe1–S7 | 2.2266(9) |
| Fe2–S1 | 2.2874(8) |
| Fe2–S2 | 2.2723(8) |
| Fe2–S3 | 2.2153(8) |
| Fe2–S5 | 2.2574(8) |
| Fe3–S1 | 2.2514(7) |
| Fe3–S3 | 2.2652(9) |
| Fe3–S4 | 2.2561(8) |
| Fe3–S6 | 2.2472(8) |
| Fe4–S2 | 2.2718(8) |
| Fe4–S3 | 2.2783(8) |
| Fe4–S4 | 2.3286(9) |
| Fe4–S8 | 2.2469(6) |
| Fe–S–Fe | 74.84(2) |
| | 74.03(2) |
| | 75.09(3) |
| | 76.54(3) |
| | 76.09(3) |
| | 74.95(3) |
| | 74.99(3) |
| | 74.02(2) |
| | 75.60(2) |
| | 76.86(3) |
| | 76.84(3) |
| | 76.24(2) |
| S–Fe–S | 105.67(3) |
| | 102.90(3) |
| | 103.29(3) |
| | 100.70(3) |
| | 103.04(3) |
| | 105.06(3) |
| | 101.01(3) |
| | 102.08(3) |
| | 103.07(3) |
| | 101.92(3) |
| | 102.18(3) |
| | 102.61(3) |
| Fe–Fe–Fe | 59.39(1) |
| | 60.32(1) |
| | 60.29(1) |
| | 61.81(1) |
| | 59.04(1) |
| | 59.15(1) |
| | 59.29(1) |
| | 61.32(1) |
| | 59.38(1) |
| | 60.66(1) |
| | 61.42(1) |
| | 57.92(1) |

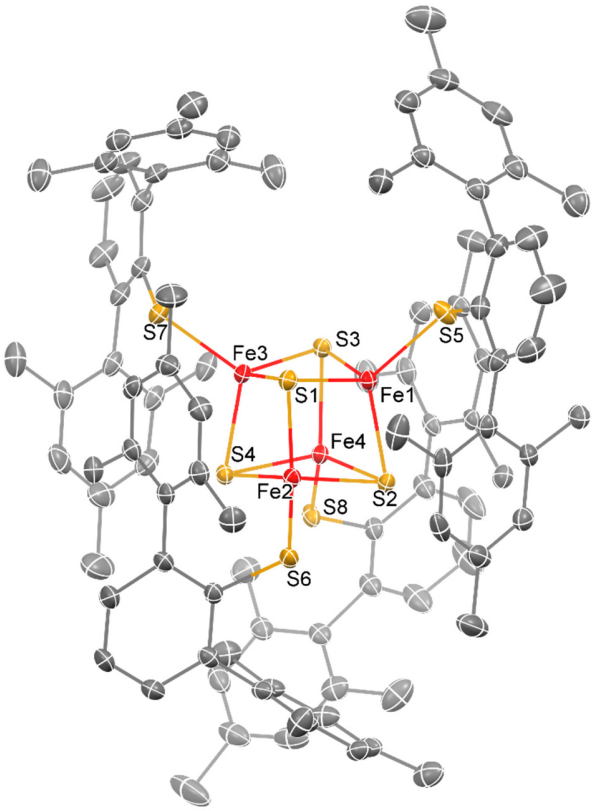


**Figure S36.**
Solid-state molecular structure of **7** in crystals of **7**·$C_6H_{18}Si_2O$. Hydrogen atoms and one co-crystallized molecule of HMDSO have been omitted for clarity; ORTEP thermal ellipsoids are shown at the 50 % probability level. Selected bond lengths and angles are summarized in Table S7.

**Table S7.**
Summary of selected bond lengths and angles for the solid-state molecular structure of compound **7**.

| property / Å or ° | 7 |
|---|---|
| Fe1–Fe2 | 2.7062(7) |
| Fe1–Fe3 | 2.7295(6) |
| Fe1–Fe4 | 2.7866(8) |
| Fe2–Fe3 | 2.7264(8) |
| Fe2–Fe4 | 2.7419(7) |
| Fe3–Fe4 | 2.8101(7) |
| Fe1–S1 | 2.2297(8) |
| Fe1–S2 | 2.2619(8) |
| Fe1–S3 | 2.2648(9) |
| Fe1–S5 | 2.197(1) |
| Fe2–S1 | 2.2585(8) |
| Fe2–S2 | 2.2395(8) |
| Fe2–S4 | 2.2132(9) |
| Fe2–S6 | 2.1905(9) |
| Fe3–S1 | 2.2472(9) |
| Fe3–S3 | 2.2319(8) |
| Fe3–S4 | 2.2608(8) |
| Fe3–S7 | 2.2015(9) |
| Fe4–S2 | 2.2383(9) |
| Fe4–S3 | 2.2840(8) |
| Fe4–S4 | 2.2712(8) |
| Fe4–S8 | 2.222(1) |
| Fe–S–Fe | 75.08(3) |
| | 76.64(3) |
| | 75.38(3) |
| | 75.55(3) |
| | 74.74(3) |
| | 76.95(3) |
| | 75.13(3) |
| | 74.16(3) |
| | 74.47(3) |
| | 76.51(3) |
| | 75.52(3) |
| | 73.91(3) |
| S–Fe–S | 102.74(3) |
| | 103.57(3) |
| | 102.50(3) |
| | 103.07(3) |
| | 102.30(3) |
| | 104.23(3) |
| | 103.84(3) |
| | 104.03(3) |
| | 103.91(3) |
| | 100.56(3) |
| | 102.43(3) |
| | 102.01(3) |
| Fe–Fe–Fe | 61.85(2) |
| | 58.80(2) |
| | 59.35(2) |
| | 60.32(2) |
| | 60.21(2) |
| | 59.47(2) |
| | 59.87(2) |
| | 61.52(2) |
| | 58.61(2) |
| | 61.24(2) |
| | 58.38(2) |
| | 60.38(2) |

**Crystallographic Identification of the Unique Iron Site in 3**

A black crystal of $K_4[Fe_4S_4(DmpS)_4]\cdot 2HMDSO$ (**3**) was selected from the mother liquor (toluene/HMDSO) and sealed under Argon in a 0.5 mm Mark tube in order to avoid decomposition upon contact to air (oxygen or moisture) or solvent loss and was quickly transferred to the diffractometer (Bruker Venture D8 diffractometer equipped with a Bruker Photon II detector) into the cold nitrogen beam (100 K). A data collection at 100 K was followed by a series of measurements at varying temperatures (125 K, 150 K, 175 K, 200 K, 225 K, 250 K and 275 K). The crystal under investigation turned out to be twinned by inversion with about 0.181(13) volume fraction of the inverted domain.

The refinements based on the 100 K data showed that the refinement of the anisotropic displacement parameters of Fe1 leads to a distinctively prolate ellipsoid with mean square atomic displacement parameters *U* of 0.0208 $Å^2$, 0.0113 $Å^2$ and 0.0111 $Å^2$, pointing to the center of the Fe-tetrahedron. This leads to an Alert G related to the Hirshfeld test (Fe1-S2: 14.5 s.u., Fe1-S1: 11.5 and 6.5 s.u.). On the level of a standard routine structure determination, solely used for determination of the connectivity, this would not be very alarming.

However, there are a several experimental observations, which led us to a more in-depth examination of the refinement:

- A polyhedron with symmetry the -4 ($S_4$) point symmetry is neither compatible with the spectroscopic data (Mössbauer & parallel mode EPR) nor with the magnetic measurements (SQUID). There has to be a symmetry breaking distortion, even though it is expected to be fairly small.
- **4** is the only compound of the whole series with a significant prolate shape of the ellipsoid for the iron atom (Tab. S8, highlighted in bold font).

**Table S8.**
Compilation of anisotropic displacement parameters $U_l$, $U_m$, $U_s$ as well as prolateness, $U_l/((U_m+U_s)/2)$, for all crystallographically detected Fe atoms in compounds **3**, **4**, **5**, **6** & **7**. The high value of prolateness for **3** is highlighted using bold font.

| | atom | $U_{large}$ ($U_l$) | $U_{medium}$ ($U_m$) | $U_{small}$ ($U_s$) | $U_l/((U_m+U_s)/2)$ |
|---|---|---|---|---|---|
| **3** | Fe1 | 0,0208 | 0,0113 | 0,0112 | **1,8489** |
| **4** | Fe1 | 0,0308 | 0,0276 | 0,0196 | 1,3051 |
| **5** | Fe1 | 0,0185 | 0,0137 | 0,0102 | 1,5481 |
| **5** | Fe2 | 0,0165 | 0,0142 | 0,0102 | 1,3525 |
| **6** | Fe1 | 0,0189 | 0,0167 | 0,016 | 1,1560 |
| **6** | Fe2 | 0,0188 | 0,0174 | 0,0163 | 1,1157 |
| **6** | Fe3 | 0,0197 | 0,0174 | 0,0163 | 1,1691 |
| **6** | Fe4 | 0,0211 | 0,0192 | 0,015 | 1,2339 |
| **7** | Fe1 | 0.0194 | 0.0162 | 0.0135 | 1.3064 |
| **7** | Fe2 | 0.0196 | 0.0170 | 0.0134 | 1.2895 |
| **7** | Fe3 | 0.0193 | 0.0168 | 0.0130 | 1.2953 |
| **7** | Fe4 | 0.0187 | 0.0158 | 0.0133 | 1.2852 |

A close inspection of the difference Fourier map shows weak, however significant negative residual electron density inside the tetrahedron while there is a positive electron density peak located outside of the Fe-tetrahedron (Fig. 37*A*,*a*). This particular residual electron density progression (positive-negative-zero-negative, when following the red line in Fig. 37*A*,*a*) from the outside of the tetrahedron through the iron atom position to the inside) is very characteristic for a case, where the positional disorder over two sites is improperly described by only one site but with a large ellipsoid. A schematic view is given in Fig. 38.

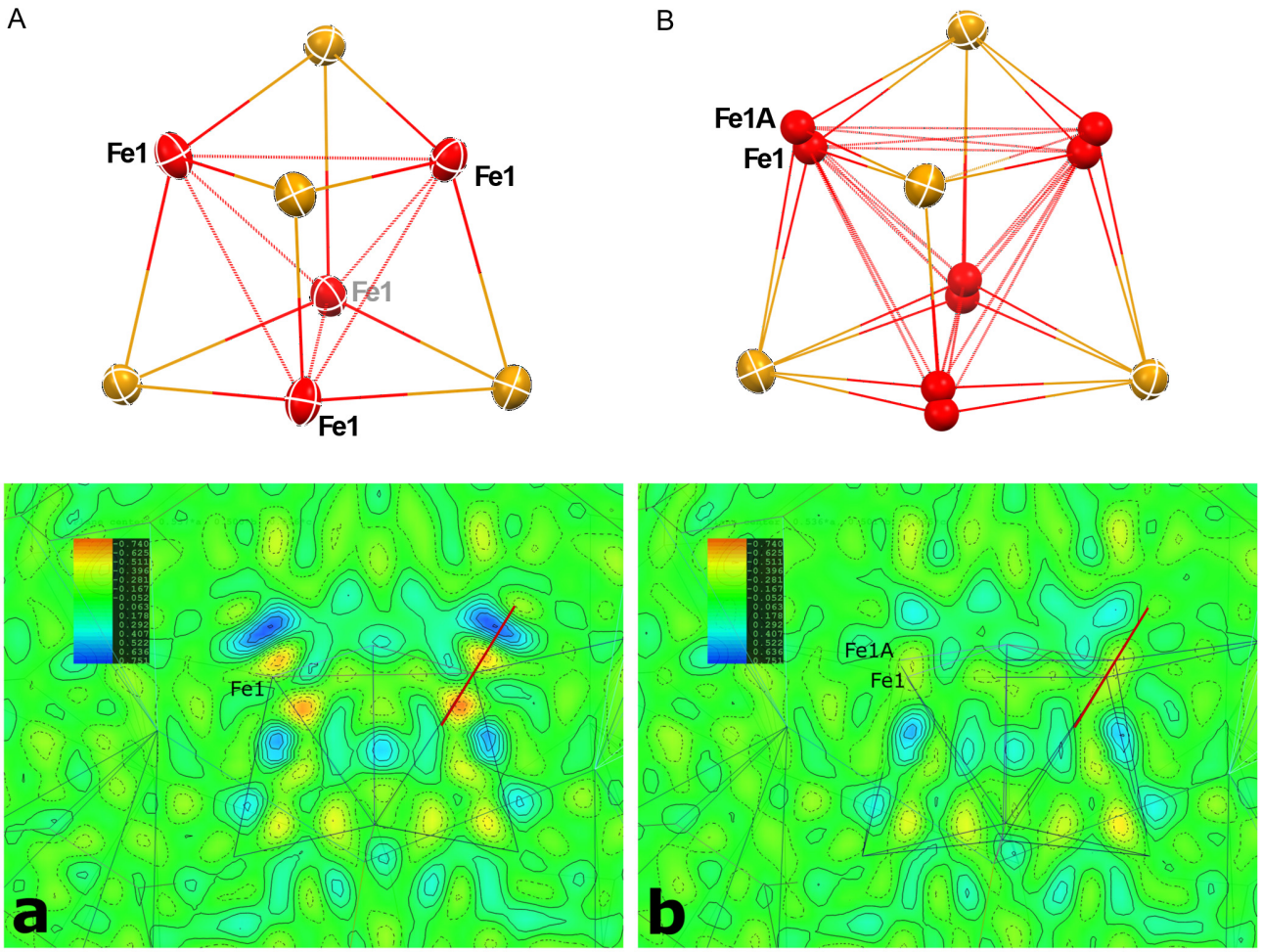


**Figure S37.**
Comparison of the central core of **3**. (*A*) Refined with one Fe-atom position and anisotropic displacement parameters. (*B*) Refined with a disordered model with two iron positions (occupancy ratio refines to about 80%:20%, the Fe-atom site with the larger occupancy is located closer to the center of the tetrahedron) and equal isotropic displacement parameters. (*a*) The difference electron density map (–0.74 e/Å$^3$ to 0.751 e/Å$^3$, iso-values in increments of 0.1147 e/Å$^3$) of a mean plane through the $Fe_4$-tetrahedron shows one area of positive (*blue*, outside the central tetrahedron) and two areas of negative electron density (*red*, one inside and a smaller one outside the central tetrahedron) close to the Fe1 position, when the displacement of the Fe-atom is described with a prolate ellipsoid with mean square atomic displacement parameters *U* of 0.0208 Å$^2$, 0.0113 Å$^2$ and 0.0111 Å$^2$. (*b*) shows the same area of the residual density when using a split model with two Fe-positions Fe1 and Fe1A and equal isotropic displacement parameters instead. The refinement converges at occupancies of 0.797(8) for Fe1 and 0.203(8) for Fe1A, respectively, with a distance Fe1–Fe1A of 0.245(4) Å). Using a split model with two disordered and partially occupied Fe-atom positions is clearly superior for a description of the observed electron density.

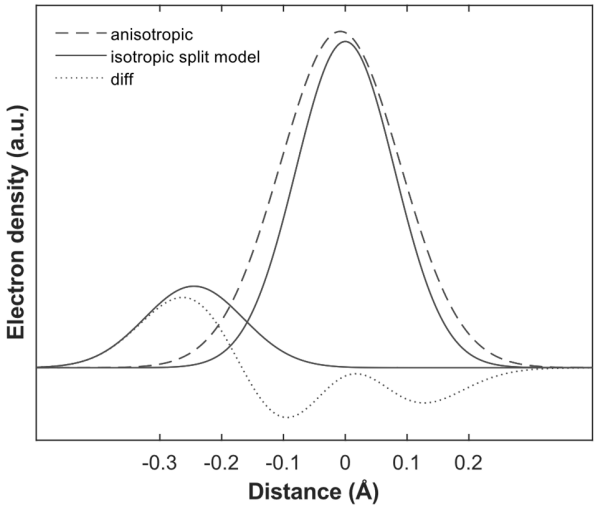


**Figure S38.** Schematic view of the electron density distributions in a disordered system with unequal occupancies 80% and 20% (solid lines) and the electron distribution calculated based on an iron atom on a single site with a larger displacement parameter (dashed) compared to the split positions (solid). The corresponding difference electron density distribution is shown as a dotted line.

Two closely located Gaussians, one representing 80 % of the electron density distribution (right solid curve) and one representing 20 % electron density (left solid curve) are described with one Gaussian representing 100 % of the electron density (dashed curve), whose maximum is close to the position of the 80 % Gaussian, but with a larger ellipsoid than necessary for a separate, individual description of the 20% and 80% Gaussians. As a result of this improper description, the resulting difference electron density (dotted curve) shows exactly the same behavior (positive-negative-zero-negative) as it is observed for the description of the disordered iron position with only one site and a too large anisotropic displacement parameter (Fig. 37*A*,*a*). This is a sign, that the ellipsoid of one iron atom position cannot properly account for the observed electron density and a description with a split position is more suitable. Indeed, when applying a split model using two partially occupied iron atom positions with a free refinement of the occupancies, the R values dropped from R1=3.66 % and wR2=7.9 % to R1=3.53 %, wR2=7.74 % and the pronounced residual electron density peaks disappeared (Fig. 37*B*,*b*). For the final refinement, the disordered split atoms were refined with isotropic parameters, because of the occurrence of large correlation matrix elements between positional parameters and displacement parameters for a refinement with anisotropic displacement parameters. Note that a description modelling the situation with two sites, individual occupancies (sum constrained to 100% occupancy) and isotropic displacement parameters constrained to be equal for both sites, needs only 8 parameters. The initial description with one site and anisotropic displacement parameters requires 9 parameters in total (three positional and 6 parameters for the ellipsoid). This means, despite employing one parameter less, the R-value drops significantly and even more importantly, the residual electron density is now flat (Fig. 37*B*,*b*), which are good signs that the disordered model is a more appropriate description of the real situation.

Altogether, the individual $Fe_4S_4$-units do not exhibit the –4 ($S_4$) point symmetry as it is imposed by the tetragonal space group $P\bar{4}2_1c$ (No. 114) when using only one fully occupied iron atom position. Rather, the statistical superposition of the distorted $Fe_4S_4$–units, disordered over four sites by adopting four different orientations, simulates the –4 symmetry (Fig. S39).

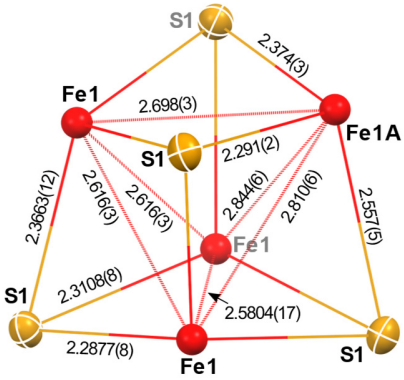


**Figure S39.**
One distorted $Fe_4S_4$-unit, containing three symmetry equivalent iron-atoms (Fe1-site with an occupancy of 0.797(8)) and one iron-atom of the Fe1A-site with an occupancy of 0.203(8). The disorder described by the split model corresponds to a superposition of this locally ordered unit in four different orientations. Distances are given in Å.

The refinement, constraining the sum of the occupancies to 1 and the isotropic displacement parameters for both split positions to be equal, converges at an occupancy ratio of 0.797(8):0.203(8) at 100 K for Fe1 and Fe1A, respectively. This Fe1-Fe1A occupancy ratio of 80:20 is slightly higher than expected for the *S*=4 ground state, where a 75:25 ratio should be adopted. Therefore, the evolution of the site occupancies of the iron positions was determined from the series of measurements performed at higher temperatures (100 K – 275 K in steps of 25 K). With increasing temperature, the intensity/sigma ratio at higher angles decreases strongly. Accordingly, the maximum resolution used for refinement was gradually decreased from 0.59 Å at 100 K and 125 K to 0.6 Å at 150 K and 175 K, 0.61 Å at 200 K and 225 K, 0.62 Å at 250 K and 0.63 Å at 275 K in order to keep the minimum *I/s* ratio above 2 even for the highest resolution shell. Nevertheless, the resolution is still very good and allowed for a reliable determination of the Fe1 site occupancy (Fig. S40). Hereby, a linear dependence of the occupancy of the Fe1-site with respect to temperature is observed, following a straight line given by the formula *occ*(Fe1)=0.0004*T*+0.748. The extrapolation to 0 K gives an occupancy of almost exactly 0.75, as it is expected for a fully occupied ground-state of *S*=4. This is in line with the temperature dependence of the effective magnetic moment, $\mu_{eff}$ (Fig. S29), which also shows a linear decrease with lower temperature until approximately 15 K.

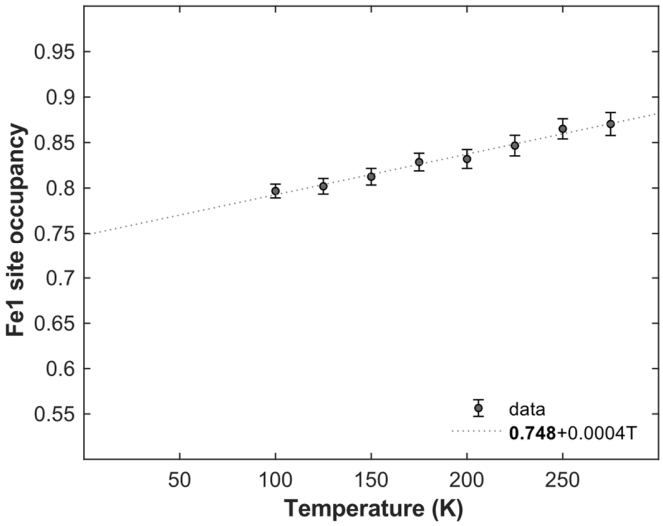


**Figure S40.**
Linear dependence of the Fe1 site occupancy in **3** with respect to temperature. Data are represented by grey circles with error bars and the grey dotted line corresponds to a linear fit.

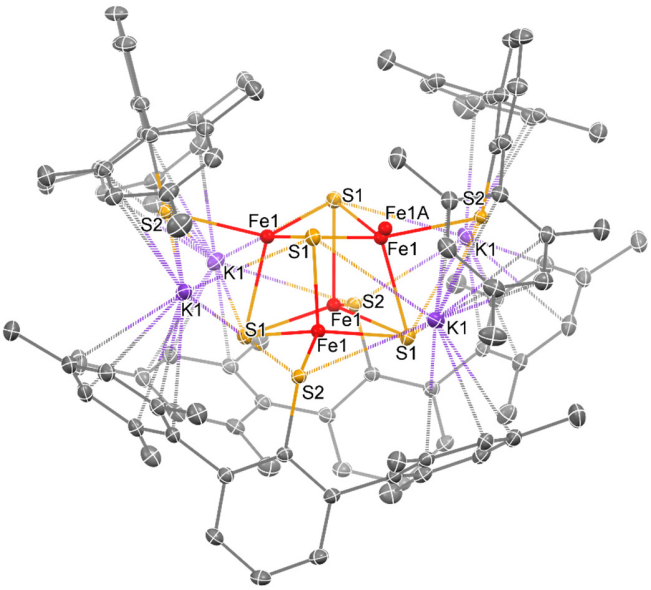


**Figure S41.**
Solid-state molecular structure of **3** in crystals of **3**·2$C_6H_{18}Si_2O$ based on the split-refinement (Fe1-site with an occupancy of 0.797(8) and Fe1A-site with an occupancy of 0.203(8)). Hydrogen atoms and two co-crystallized molecules of HMDSO have been omitted for clarity; ORTEP thermal ellipsoids are shown at the 50 % probability level. Selected bond lengths and angles are summarized in Tab. S6.

**Table S9.**
Selected interatomic distances within the $Fe_4S_4$-unit of **3** consisting of three Fe1 atom sites and one Fe1A site. In the $Fe_4S_4$-unit refined with only one fully occupied Fe1 atom site and exhibiting the –4 ($S_4$) symmetry the Fe-Fe distances (in Å) are 2.6882(5), 2.6179(5) and 2.6883(5) and the Fe–S1 distances (in Å) are 2.3983(5), 2.2864(6) and 2.3200(6).

| atom 1 | atom 2 | distance / Å |
|---|---|---|
| Fe1A | Fe1 | 2.698(3) |
| | Fe1 | 2.844(6) |
| | Fe1 | 2.810(6) |
| Fe1 | Fe1 | 2.616(3) |
| | Fe1 | 2.5804(17) |
| | Fe1 | 2.616(3) |
| Fe1A | S1 | 2.291(2) |
| | S1 | 2.557(5) |
| | S1 | 2.374(3) |
| Fe1 | S1 | 2.2877(8) |
| | S1 | 2.3108(8) |
| | S1 | 2.3663(12) |
| Fe1 | S1 | 2.2877(8) |
| | S1 | 2.3108(8) |
| | S1 | 2.3663(12) |
| Fe1 | S1 | 2.3663(12) |
| | S1 | 2.2877(8) |
| | S1 | 2.3108(8) |
| Fe1 | S2 | 2.373(1) |
| Fe1A | S2 | 2.227(3) |

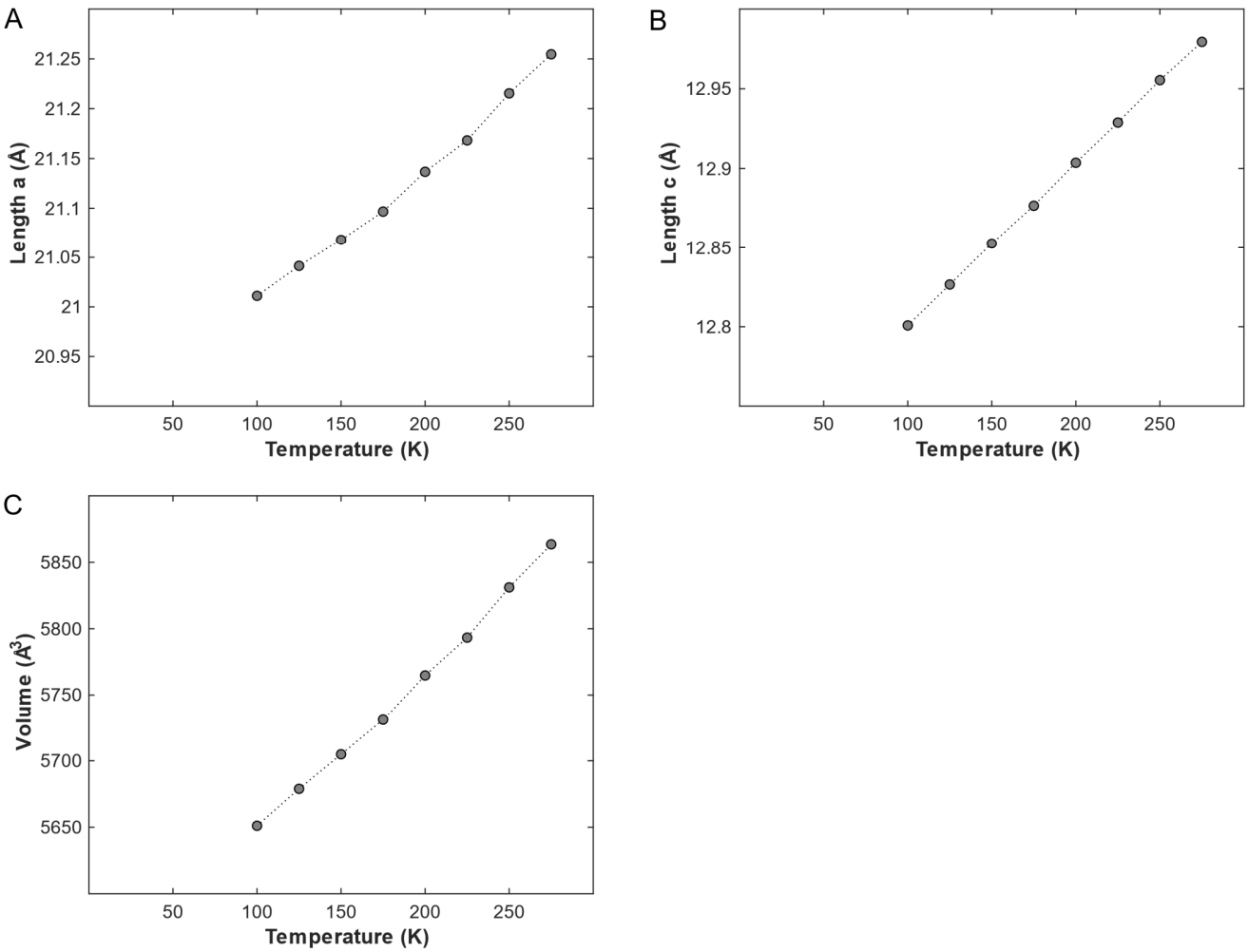


**Figure S42.**
Temperature dependence of the unit cell parameters of compound **3**. (*A*) Unit cell length *a* (where *a*=*b*) plotted *versus* temperature *T*. (*B*) Unit cell length *c* plotted *versus* temperature *T*. (*C*) Unit cell volume *V* plotted *versus* temperature *T*.

**Table S10.**
Crystallographic data, data collection and refinement details for compounds **3**-**7**.

| **parameter** | **1** | **2** | **3** | **4** | **5** | **6** | **7** |
|---|---|---|---|---|---|---|---|
| empiric formula | $FeS_2C_{48}H_{50}K$ $\cdot C_7H_8$ | $C_{96}H_{100}Fe_2S_6K_2$ $\cdot C_4H_{10}O$ | $C_{96}H_{100}Fe_4S_8K_4$ $\cdot 2C_6H_{18}OSi_2$ | $C_{96}H_{100}Fe_4S_8K_3$ $\cdot 2C_6H_{18}OSi_2$ | $C_{96}H_{100}Fe_4S_8K_2$ $\cdot 2C_6H_{18}OSi_2$ | $C_{96}H_{100}Fe_4S_8K$ $\cdot C_7H_8$ | $C_{96}H_{100}Fe_4S_8$ $\cdot C_6H_{18}OSi_2$ |
| M [g mol$^{-1}$] | 878.08 | 1710.13 | 2214.80 | 2175.70 | 2136.60 | 1864.87 | 1896.02 |
| crystal size [mm] | 0.33 × 0.099 × 0.067 | 0.553 × 0.352 × 0.196 | 0.224 x 0.248 x 0.744 | 0.5 x 0.02 x 0.02 | 0.339 x 0.112 x.0.096 | 0.18 x 0.11 x 0.09 | 0.41 x 0.08 x 0.08 |
| temperature | 100 K | 100 K | 100 K | 100 K | 100 K | 100 K | 100 K |
| crystal system | *monoclinic* | *monoclinic* | *tetragonal* | *tetragonal* | *orthorhombic* | *triclinic* | *orthorhombic* |
| space group (no.) | $P2_1/c$ (14) | $P2_1/n$ (14) | $P\bar{4}2_1c$ (114) | $P\bar{4}2_1c$ (114) | $P2_12_12$ (18) | $P\bar{1}$ (2) | $P2_12_12_1$ (19) |
| a [Å] | 15.1439(5) | 13.3169(6) | 21.0111(6) | 20.9190(8) | 20.8338(10) | 12.8103(12) | 12.9675(2) |
| b [Å] | 16.3197(5) | 15.0671(7) | 21.0111(6) | 20.9190(8) | 20.8665(9) | 16.2213(14) | 25.8619(5) |
| c [Å] | 19.3486(6) | 44.064(2) | 12.8008(4) | 12.8022(4) | 12.8089(5) | 24.175(2) | 29.6152(5) |
| $\alpha$ [°] | 90 | 90 | 90 | 90 | 90 | 83.640(2) | 90 |
| $\beta$ [°] | 104.766(3) | 93.254(2) | 90 | 90 | 90 | 88.369(2) | 90 |
| $\gamma$ [°] | 90 | 90 | 90 | 90 | 90 | 69.107(2) | 90 |
| V [Å$^3$] | 4624.0(3) | 8827.1(7) | 5651.1(4) | 5602.3(5) | 5568.4(4) | 4664.0(7) | 9931.9(3) |
| Z, Z' | 4, 1 | 4, 1 | 2, 0.25 | 2, 0.25 | 2, 0.5 | 2, 1 | 4, 1 |
| $\mu$ [mm$^{-1}$] | 0.543 | 0.613 | 0.886 | 0.857 | 0.824 | 0.880 | 0.810 |
| F(000) | 1860.0 | 3616.0 | 2328.0 | 2290.0 | 2252.0 | 1954.0 | 3992.0 |
| abs. corr. | SCALE3 ABSPACK | SADABS | SADABS | SADABS | SADABS | SADABS | SCALE3 ABSPACK |
| $T_{min}$; $T_{max}$ | 0.9063; 1.0000 | 0.7479; 0.8503 | 0.558; 0.826 | 0.6715; 0.7452 | 0.6869; 0.7457 | 0.7000; 0.7454 | 0.4576; 1.0000 |
| 2$\theta$-range [°] | 3.312 to 50.698 | 4.414 to 80.186 | 4.334 to 74.068 | 4.354 to 50.952 | 4.212 to 56.592 | 2.704 to 52.876 | 5.42 to 61.016 |
| coll. refl. | 99590 | 315027 | 159601 | 146036 | 175854 | 114375 | 86891 |
| indep. refl. | 8481 | 54774 | 14407 | 5211 | 13837 | 19118 | 30129 |
| no. ref. param. | 545 | 1026 | 303 | 303 | 597 | 1134 | 1084 |
| $wR_2$ | 0.0974 | 0.0961 | 0.0772 | 0.0609 | 0.0646 | 0.0871 | 0.0809 |
| $R_1(F_0 \geq 4.0\sigma(F))$ | 0.0501 | 0.0437 | 0.0353 | 0.0305 | 0.0333 | 0.0394 | 0.0373 |
| GooF $F^2$ | 1.022 | 1.120 | 1.111 | 1.145 | 1.105 | 1.037 | 1.022 |
| $\Delta\rho$ (max; min) [eÅ$^3$] | 0.35/-0.41 | 0.60/-0.71 | 0.55/-0.36 | 0.21/-0.22 | 0.33/-0.50 | 0.46/-0.33 | 0.64/-0.49 |
| CSD number | 2124640 | 2124636 | 2124635 | 2124638 | 2124637 | 2124639 | 2167405 |

**Table S11.**
Summary of structural parameters of the redox series **3-7**.

| **property** | $[Fe_4S_4]^{4+}$ (**7**) | $[Fe_4S_4]^{3+}$ (**6**) | $[Fe_4S_4]^{2+}$ (**5**) | $[Fe_4S_4]^{1+}$ (**4**) | $[Fe_4S_4]^{0}$ (**3**) |
|---|---|---|---|---|---|
| Fe–Fe / Å | 2.7062(7) | 2.8350(7) | 2.7490(9) | 2.6799(6) | 2.844(6) |
| | 2.7295(6) | 2.8144(6) | 2.7729(9) | 2.7307(7) | 2.698(3) |
| | 2.7866(8) | 2.7356(5) | 2.7163(9) | | 2.810(6) |
| | 2.7264(8) | 2.7616(7) | 2.7303(9) | | 2.616(3) |
| | 2.7419(7) | 2.7582(6) | | | 2.616(3) |
| | 2.8101(7) | 2.7609(6) | | | 2.5804(17) |
| Fe–Fe av. / Å | 2.75(1) | 2.78(1) | 2.75(1) | 2.71(1) | 2.69(2) |
| Fe–S av. / Å | 2.25(2) | 2.27(2) | 2.29(2) | 2.31(2) | 2.34(2) |
| Fe–SR av. / Å | 2.20(2) | 2.24(1) | 2.28(1) | 2.30(1) | 2.34(2) |
| $V(Fe_4)$ / Å$^3$ | 2.45 | 2.52 | 2.43 | 2.35 | 2.29 |
| $V(S_4)$ / Å$^3$ | 5.14 | 5.26 | 5.54 | 5.87 | 6.25 |

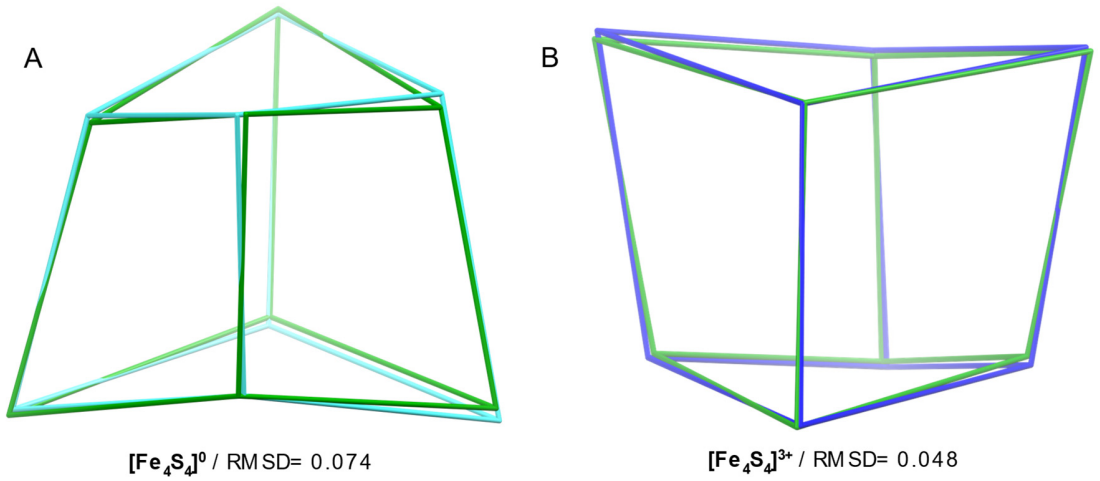


**Figure S43.**
Root-mean-squared distance (RMSD) minimized overlays of the solid-state molecular structures of the $Fe_4S_4$-units of, (*A*), compound **3** (*cyan*) with 1G1M (18) (*green*) and, (*B*), compound **6** (*blue*) with 1HPI (25) (*green*), respectively. Images were generated using the Mercury® program suite.

**Table S12.**
Summary of average geometric parameters and $^{57}$Fe Mössbauer isomer shifts for a selection of $Fe_4S_4$ complexes of synthetic and biological origin. $\delta$ values are given for temperatures of 77-140 K, depending on data availability. Note that this is not an exhaustive compilation, but one aiming toward an illustrative comparison, covering all oxidation states relevant in biological systems to date. These values are issued in Fig. 4*C* of the main text.

| **system / PDB code** | $[Fe_4S_4]^n$ | V($Fe_4$) / Å$^3$ | V($S_4$) / Å$^3$ | Fe–$S_{av.}$ / Å | Fe–$Fe_{av.}$ / Å | $\delta_{av.}$ / mm·s$^{-1}$ | **ref.** |
|---|---|---|---|---|---|---|---|
| $[Fe_4S_4(DmpS)_4]$ | 4+ | 2.45 | 5.14 | 2.25(2) | 2.75(1) | 0.32 | *this work* |
| $K[Fe_4S_4(DmpS)_4]$ | 3+ | 2.52 | 5.26 | 2.27(2) | 2.78(1) | 0.38 | *this work* |
| $K_2[Fe_4S_4(DmpS)_4]$ | 2+ | 2.43 | 5.54 | 2.29(2) | 2.75(1) | 0.46 | *this work* |
| $K_3[Fe_4S_4(DmpS)_4]$ | 1+ | 2.35 | 5.87 | 2.31(2) | 2.71(1) | 0.52 | *this work* |
| $K_4[Fe_4S_4(DmpS)_4]$ | 0 | 2.29 | 6.25 | 2.34(2) | 2.69(2) | 0.62 | *this work* |
| $[Fe_4S_4(i\mathrm{Pr}^{NHC})_4]$ | 0 | 2.27 | 6.14 | 2.33(2) | 2.68(6) | 0.60 | (26) |
| $[Fe_4S_4(i\mathrm{Pr}^{NHC})_4](BPh_4)$ | 1+ | 2.37 | 5.60 | 2.29(3) | 2.71(2) | - | (27) |
| $(^n\mathrm{Bu}_4\mathrm{N})_4[Fe_4S_4(CN)_4]$ | 0 | 2.25 | 6.21 | 2.33(2) | 2.67(3) | 0.65 | (28) |
| $(^n\mathrm{Bu}_4\mathrm{N})_3[Fe_4S_4(CN)_4]$ | 1+ | 2.34 | 5.64 | 2.29(1) | 2.71(2) | 0.49 | (28) |
| $[Fe_4S_4(SAr)_4]^{3-}$ (5 examples) | 1+ | av.: **2.42**<br>max: 2.46<br>min: 2.38 | av.: **5.74**<br>max: 5.76<br>min: 5.70 | av.: **2.31**<br>max: 2.37<br>min: 2.24 | av.: **2.74**<br>max: 2.82<br>min: 2.71 | - | (29) |
| $[Fe_4S_4(SAr)_4]^{2-}$ (11 examples) | 2+ | av.: **2.41**<br>max: 2.47<br>min: 2.38 | av.: **5.51**<br>max: 5.61<br>min: 5.44 | av.: **2.28**<br>max: 2.33<br>min: 2.22 | av.: **2.73**<br>max: 2.78<br>min: 2.70 | - | (29) |
| $[Fe_4S_4(SAr)_4]^{1-}$ (8 examples) | 3+ | av.: **2.49**<br>max: 2.58<br>min: 2.40 | av.: **5.28**<br>max: 5.36<br>min: 5.22 | av.: **2.27**<br>max: 2.31<br>min: 2.22 | av.: **2.76**<br>max: 2.81<br>min: 2.72 | - | (15, 29) |
| $[Fe_4S_4(SAlkyl)_4]^{3-}$ (5 examples) | 1+ | av.: **2.49**<br>max: 2.51<br>min: 2.45 | av.: **5.77**<br>max: 5.81<br>min: 5.71 | av.: **2.32**<br>max: 2.34<br>min: 2.27 | av.: **2.76**<br>max: 2.79<br>min: 2.72 | - | (29) |
| $[Fe_4S_4(SAlkyl)_4]^{2-}$ (17 examples) | 2+ | av.: **2.44**<br>max: 2.55<br>min: 2.37 | av.: **5.52**<br>max: 5.59<br>min: 5.46 | av.: **2.29**<br>max: 2.34<br>min: 2.23 | av.: **2.75**<br>max: 2.81<br>min: 2.70 | - | (29) |
| 1G1M | 0 | 2.17 | 6.17 | 2.33 | 2.65 | - | (18) |
| 1CP2 | 1+ | 2.14 | 5.98 | 2.30 | 2.63 | - | (30) |
| 1G5P | 1+ | 2.22 | 6.00 | 2.31 | 2.66 | - | (18) |
| 1HLQ (3 clusters) | 2+ | 2.35 | 5.74 | 2.31 | 2.71 | - | (31) |
| 1HIP | 3+ | 2.40 | 5.16 | 2.25 | 2.73 | - | (32) |
| 1HPI | 3+ | 2.37 | 5.23 | 2.25 | 2.72 | | (25) |
| 2FGO (2clusters) | 2+ | 2.43 | 5.57 | 2.29 | 2.75 | - | (33) |
| 1NIP | 2+ | 2.33 | 5.84 | 2.27 | 2.71 | - | (34) |
| 1IQZ | 2+ | 2.38 | 5.62 | 2.29 | 2.73 | - | (35) |
| *Av2* FeP $[Fe_4S_4]^0$ | 0 | - | - | - | - | 0.65 | (36) |
| *Av2* FeP $[Fe_4S_4]^{1+}$ | 1+ | - | - | - | - | 0.55, 0.56 | (37) |
| *Av2* FeP $[Fe_4S_4]^{2+}$ | 2+ | - | - | - | - | 0.45 | (37) |
| *Chromatium* HiPIP $[Fe_4S_4]^{2+}$ | 2+ | - | - | - | - | 0.42 | (38) |
| *Chromatium* HiPIP $[Fe_4S_4]^{3+}$ | 3+ | - | - | - | - | 0.36 | (38) |
| *E. coli* sulfite reductase $[Fe_4S_4]^{1+}$ | 1+ | - | - | - | - | 0.56 | (37) |
| *B. stearothermophilus* Fd $[Fe_4S_4]^{1+}$ | 1+ | - | - | - | - | 0.54 | (37, 39) |
| *B. stearothermophilus* Fd $[Fe_4S_4]^{2+}$ | 2+ | - | - | - | - | 0.43 | (39) |

**Table S13.**
Summary of detailed bond lengths of all-ferrous FeS cubanes of synthetic and biological origin reported in literature.

| **property** | $[Fe_4S_4]^0$ (**3**) | $[Fe_4S_4]^0_{CN}$ | $[Fe_4S_4]^0_{NHC}$ | $[Fe_4S_4]^0_{DFT}$ | $[Fe_4S_4]^0_{DFT}$ | $[Fe_4S_4]^0_{EXAFS}$ | 1G1M |
|---|---|---|---|---|---|---|---|
| Fe–Fe / Å | 2.844(6) | 2.6756(8) | 2.719(1) | 2.866 | 2.56 | 2.562 (x3) | 2.79 |
| | 2.698(3) | 2.627(1) | 2.603(1) | 2.626 | 2.56 | 2.748 (x3) | 2.67 |
| | 2.810(6) | 2.6825(8) | 2.675(1) | 2.756 (x4) | 2.77 | | 2.69 |
| | 2.616(3) | 1.696(1) | 2.710(1) | | 2.58 | | 2.57 |
| | 2.616(3) | | 2.764(1) | | 2.76 | | 2.66 |
| | 2.5804(17) | | 2.613(1) | | 2.71 | | 2.54 |
| Fe–Fe av. / Å | 2.69(2) | 2.67(3) | 2.68(6) | 2.75 | 2.66 | 2.66 | 2.65 |
| Fe–S / Å | 2.291(2) | 2.325(1) | 2.337(1) | 2.378 (x8) | 2.37 | 2.213 (x3) | |
| | 2.557(5) | 2.364(1) | 2.338(1) | 2.357 (x4) | 2.37 | 2.324 (x9) | |
| | 2.374(3) | 2.326(1) | 2.328(1) | | 2.42 | | |
| | 2.2877(8) | 2.334(1) | 2.291(1) | | 2.37 | | |
| | 2.3108(8) | 2.337(1) | 2.334(1) | | 2.38 | | |
| | 2.3663(12) | | 2.308(1) | | 2.37 | | |
| | 2.2877(8) | | 2.318(1) | | 2.38 | | |
| | 2.3108(8) | | 2.370(1) | | 2.38 | | |
| | 2.3663(12) | | 2.344(1) | | 2.43 | | |
| | 2.3663(12) | | 2.335(1) | | 2.33 | | |
| | 2.2877(8) | | 2.334(1) | | 2.32 | | |
| | 2.3108(8) | | 2.327(1) | | 2.35 | | |
| Fe–S av. / Å | 2.34(2) | 2.33(2) | 2.33(2) | 2.37 | 2.37 | 2.30 | 2.33 |
| **ref.** | *this work* | (28) | (26) | (40) | (41) | (41) | (18) |

**Determination of Tetrahedron Volume**

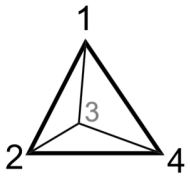


**Figure S44.**
Schematic representation of a tetrahedron with vertices 1, 2, 3 and 4.

The volumes, $V$, of the $Fe_4$, respectively $S_4$-core tetrahedra of compounds **3**-**7** were calculated using the *Cayley-Menger determinant*, as follows:

$$288 \cdot V^2 = \begin{vmatrix} 0 & 1 & 1 & 1 & 1 \\ 1 & 0 & d_{12}^2 & d_{13}^2 & d_{14}^2 \\ 1 & d_{12}^2 & 0 & d_{23}^2 & d_{24}^2 \\ 1 & d_{13}^2 & d_{23}^2 & 0 & d_{34}^2 \\ 1 & d_{14}^2 & d_{24}^2 & d_{34}^2 & 0 \end{vmatrix} \quad ,$$

where $d_{ij}$ denote the distances between vertices as drawn in Fig. S44. As there are no uncertainties given in literature, the values were considered without $3\sigma$ from the X-ray diffraction data and rounded to the second decimal. Table S12 summarizes all the values considered for synthetic models in the main text. Data was taken from the corresponding *CIF* files as published. Data for the aromatic thiolate supported clusters denoted $[Fe_4S_4(SAr)_4]^{1-/2-/3-}$ have been taken from ref. (15, 29). For biological structures, the volumes and bond lengths have been used as published. For RMSD minimized overlays, data was downloaded directly from the *PDB* database.

**Supplementary References**


1. D. L. J. Broere, I. Čorić, A. Brosnahan, P. L. Holland, Quantitation of the THF Content in $Fe[N(SiMe_3)_2]_2 \cdot xTHF$. *Inorg. Chem.* **56**, 3140-3143 (2017).
2. Q. Zhu, D. E. Graff, R. R. Knowles, Intermolecular Anti-Markovnikov Hydroamination of Unactivated Alkenes with Sulfonamides Enabled by Proton-Coupled Electron Transfer. *J. Am. Chem. Soc.* **140**, 741-747 (2018).
3. C. J. F. Du, H. Hart, K. K. D. Ng, A One-Pot Synthesis of m-Terphenyls via a Two-Aryne sequence. *J. Org. Chem.* **51**, 3162-3165 (1986).
4. Y. Ohki, Y. Ikagawa, K. Tatsumi, Synthesis of New [8Fe-7S] Clusters: A Topological Link between the Core Structures of P-Cluster, FeMo-co, and FeFe-co of Nitrogenases. *J. Am. Chem. Soc.* **129**, 10457-10465 (2007).
5. L. M. Viculis, J. J. Mack, O. M. Mayer, H. T. Hahn, R. B. Kaner, Intercalation and exfoliation routes to graphite nanoplatelets. *J. Mater. Chem.* **15**, 974-974 (2005).
6. D. Coucouvanis, "Useful Reagents and Ligands" in Inorganic Syntheses. (2002), https://doi.org/10.1002/0471224502.ch2, pp. 75-121.
7. S. Stoll, A. Schweiger, An adaptive method for computing resonance fields for continuous-wave EPR spectra. *Chem. Phys. Lett.* **380**, 464-470 (2003).
8. M. Carboni *et al.*, Biologically Relevant Heterodinuclear Iron–Manganese Complexes. *Inorg. Chem.* **51**, 10447-10460 (2012).
9. J. J. Ellison, K. Ruhlandt-Senge, P. P. Power, Synthesis and Characterization of Thiolato Complexes with Two-Coordinate Iron(II). *Angew. Chem. Int. Ed.* **33**, 1178-1180 (1994).
10. C. J. Pickett, A simple hydrocarbon electrolyte: Completing the electron-transfer series $[Fe_4S_4(SPh)_4]^{1-/2-/3-/4-}$. *J. Chem. Soc., Chem. Commun.*, 323-326 (1985).
11. M. Niemeyer, P. P. Power, Donor-Free Alkali Metal Thiolates: Synthesis and Structure of Dimeric, Trimeric, and Tetrameric Complexes with Sterically Encumbered Terphenyl Substituents. *Inorg. Chem.* **35**, 7264-7272 (1996).
12. J. Pratt *et al.*, Effects of Remote Ligand Substituents on the Structures, Spectroscopic, and Magnetic Properties of Two-Coordinate Transition-Metal Thiolate Complexes. *Inorg. Chem.* **57**, 6491-6502 (2018).
13. I. Čorić, B. Q. Mercado, E. Bill, D. J. Vinyard, P. L. Holland, Binding of dinitrogen to an iron–sulfur–carbon site. *Nature* **526**, 96-99 (2015).
14. J. Cambray, R. W. Lane, A. G. Wedd, R. W. Johnson, R. H. Holm, Chemical and electrochemical interrelationships of the 1-Fe, 2-Fe, and 4-Fe analogs of the active sites of iron-sulfur proteins. *Inorg. Chem.* **16**, 2565-2571 (1977).
15. K. Tanifuji *et al.*, A convenient route to synthetic analogues of the oxidized form of high-potential iron-sulfur proteins. *Inorg. Chem.* **53**, 4000-4009 (2014).
16. S. C. Lee, W. Lo, R. H. Holm, Developments in the Biomimetic Chemistry of Cubane-Type and Higher Nuclearity Iron–Sulfur Clusters. *Chem. Rev.* **114**, 3579-3600 (2014).
17. G. Moula, T. Matsumoto, M. E. Miehlich, K. Meyer, K. Tatsumi, Synthesis of an All-Ferric Cuboidal Iron–Sulfur Cluster $[Fe^{III4}S_4(SAr)_4]$. *Angew. Chem. Int. Ed.* **57**, 11594-11597 (2018).
18. P. Strop *et al.*, Crystal structure of the all-ferrous $[4Fe\text{-}4S]^0$ form of the nitrogenase iron protein from Azotobacter vinelandii. *Biochemistry* **40**, 651-656 (2001).
19. D. Sehnal *et al.*, Mol* Viewer: modern web app for 3D visualization and analysis of large biomolecular structures. *Nucleic Acids Res.* **49**, W431-W437 (2021).
20. Y. Ohki *et al.*, Synthetic analogues of $[Fe_4S_4(Cys)_3(His)]$ in hydrogenases and $[Fe_4S_4(Cys)_4]$ in HiPIP derived from all-ferric $[Fe_4S_4(N(SiMe_3)_2)_4]$. *Proceedings of the National Academy of Sciences* **108**, 12635-12640 (2011).
21. G. Sheldrick, A short history of SHELX. *Acta Crystallogr. Sect. A: Found. Crystallogr.* **64**, 112-122 (2008).
22. G. Sheldrick, Crystal structure refinement with SHELXL. *Acta Crystallogr. Sect. C: Cryst. Struct. Commun.* **71**, 3-8 (2015).
23. G. M. Sheldrick, SHELXT - Integrated space-group and crystal-structure determination. *Acta Crystallogr. Sect. A: Found. Crystallogr.* **71**, 3-8 (2015).
24. O. V. Dolomanov, L. J. Bourhis, R. J. Gildea, J. A. K. Howard, H. Puschmann, OLEX2: A complete structure solution, refinement and analysis program. *J. Appl. Crystallogr.* **42**, 339-341 (2009).
25. M. M. Benning, T. E. Meyer, I. Rayment, H. M. Holden, Molecular Structure of the Oxidized High-Potential Iron-Sulfur Protein Isolated from Ectothiorhodospira vacuolata. *Biochemistry* **33**, 2476-2483 (1994).

26. L. Deng, R. H. Holm, Stabilization of Fully Reduced Iron−Sulfur Clusters by Carbene Ligation: The $[Fe_nS_n]^0$ Oxidation Levels (n=4,8). *J. Am. Chem. Soc.* **130**, 9878-9886 (2008).
27. A. C. Brown, D. L. M. Suess, Controlling Substrate Binding to $Fe_4S_4$ Clusters through Remote Steric Effects. *Inorg. Chem.* **58**, 5273-5280 (2019).
28. T. A. Scott, C. P. Berlinguette, R. H. Holm, H. C. Zhou, Initial synthesis and structure of an all-ferrous analogue of the fully reduced $[Fe_4S_4]^0$ cluster of the nitrogenase iron protein. *Proc. Natl. Acad. Sci. U.S.A.* **102**, 9741-9744 (2005).
29. L. L. Tan, R. H. Holm, S. C. Lee, Structural analysis of cubane-type iron clusters. *Polyhedron* **58**, 206-217 (2013).
30. J. L. Schlessman, D. Woo, L. Joshua-Tor, J. B. Howard, D. C. Rees, Conformational variability in structures of the nitrogenase iron proteins from Azotobacter vinelandii and Clostridium pasteurianum. *J. Mol. Biol.* **280**, 669-685 (1998).
31. A. Gonzalez, S. Benini, S. Ciurli, Structure of Rhodoferax fermentans high-potential iron-sulfur protein solved by MAD. *Acta Crystallogr. Sect. D. Biol. Crystallogr.* **59**, 1582-1588 (2003).
32. C. W. Carter *et al.*, Two-Angstrom Crystal Structure of Oxidized Chromatium High Potential Iron Protein. *J. Biol. Chem.* **249**, 4212-4225 (1974).
33. P. Giastas *et al.*, The structure of the 2[4Fe–4S] ferredoxin from Pseudomonas aeruginosa at 1.32-Å resolution: comparison with other high-resolution structures of ferredoxins and contributing structural features to reduction potential values. *J. Biol. Inorg. Chem.* **11**, 445 (2006).
34. M. M. Georgiadis *et al.*, Crystallographic structure of the nitrogenase iron protein from Azotobacter vinelandii. *Science* **257**, 1653-1659 (1992).
35. K. Fukuyama, T. Okada, Y. Kakuta, Y. Takahashi, Atomic resolution structures of oxidized [4fe-4s] ferredoxin from Bacillus thermoproteolyticus in two crystal forms: systematic distortion of [4fe-4s] cluster in the protein. *J. Mol. Biol.* **315**, 1155-1166 (2002).
36. S. J. Yoo, H. C. Angove, B. K. Burgess, M. P. Hendrich, E. Münck, Mossbauer and integer-spin EPR studies and spin-coupling analysis of the $[4Fe\text{-}4S]^0$ cluster of the Fe protein from Azotobacter vinelandii nitrogenase. *J. Am. Chem. Soc.* **121**, 2534-2545 (1999).
37. P. A. Lindahl, E. P. Day, T. A. Kent, W. H. Orme-Johnson, E. Münck, Mössbauer, EPR, and magnetization studies of the Azotobacter vinelandii Fe protein. Evidence for a $[4Fe\text{-}4S]^{1+}$ cluster with spin $S$=3/2. *J. Biol. Chem.* **260**, 11160-11173 (1985).
38. D. P. E. Dickson *et al.*, Mössbauer effect in the high-potential iron–sulphur protein from Chromatium. Evidence for the state of the iron atoms. *Biochem. J* **139**, 105-108 (1974).
39. P. Middleton, D. P. E. Dickson, C. E. Johnson, J. D. Rush, Interpretation of the Mössbauer Spectra of the Four-Iron Ferredoxin from Bacillus stearothermophilus. *Eur. J. Biochem.* **88**, 135-141 (1978).
40. R. A. Torres, T. Lovell, L. Noodleman, D. A. Case, Density functional and reduction potential calculations of $Fe_4S_4$ clusters. *J. Am. Chem. Soc.* **125**, 1923-1936 (2003).
41. D. Mitra *et al.*, Characterization of [4Fe-4S] Cluster Vibrations and Structure in Nitrogenase Fe Protein at Three Oxidation Levels via Combined NRVS, EXAFS, and DFT Analyses. *J. Am. Chem. Soc.* **135**, 2530-2543 (2013).